Interaction between mantle-derived magma and lower arc crust: quantitative reactive melt flow modeling using STyx

Nicolas Riel[1*], Pierre Bouilhol[1,2], Jeroen van Hunen[1], Julien Cornet[1], Valentina Magni[1,3], Vili Grigorova[1] and Mirko Velic[4].

[1]Department of Earth Sciences, Durham University, Science Labs, United Kingdom.

[2]Centre de Recherches Pétrographiques et Géochimiques, Université de Lorraine, UMR 7358, 54500 Vandoeuvre-lès-Nancy, France

[3]Department of Geosciences, University of Oslo, Norway

[4]School of Earth, Atmosphere and Environment, Monash University, Melbourne, Victoria, Australia

[*]Now at Department of Earth Science, Bergen University, Bergen, Norway

Accepted for publication in Geological Society of London Special Publication:

"Metamorphic Geology: Microscale to Mountain Belts" Editors: Ferrero, S., Lanari, P., Goncalves, P., Grosch, E.G.

Doi:/10.1144/SP478.6

Abstract

The magmatic processes occurring in the lowermost arc crust plays a major role in the evolution of mantle wedge derived melt. Geological evidence indicate that mantle-derived magmas and in situ products of lower crust partial melting are reacting in a pervasive melt system, and are eventually extracted toward higher level of the crust. Resolving the relative contribution of mantle-derived magma and partial melting products of pre-existing crust is essential to: (1) quantify crustal growth rate, (2) better understand the compositional range of arc magmatic series and (3) constrain the chemical differentiation of the lower crust. In this study, we present STyx, a new modeling tool, coupling melt and heat flow with petrology to explore the dynamics of storage, transfer and hybridization of melts in complex liquid/rock systems. We perform three models representing a magmatic event affecting an amphibolitic lower arc crust in order to quantify the relative contribution between partial melting of the pre-existing crust and fractional crystallization from mantle-derived hydrous-magma. Our models demonstrate that most of the differentiated arc crust is juvenile, deriving from the differentiation of mantle melts, and that pre-existing crust does not significantly contribute to the total volume of magmatic products.

1. Introduction

The generation of felsic crust is widely attributed to two main processes: differentiation of primary magmas by crystallization within the crust or uppermost mantle (e.g., Grove et al., 2002, 2003; Jagoutz & Kelemen, 2015) and partial melting of older crustal rocks (e.g., Rapp & Watson, 1995). The extraction of melt from deep crust and its transfer in the upper crust is the principal process by which continents have become differentiated into a

more mafic, residual lower crust and a more felsic, hydrated and incompatible element-enriched upper crust (Bergantz, 1989; Brown, 2013). Conceptually, the lower crust magmatic source region is regarded as the melting, assimilation, storage and hybridization 'MASH' zone (Hildreth & Moorbath, 1988) or as the deep crust hot zone 'DCHZ' (Annen et al., 2006), where mantle and melt-derived melt mix and interact with the lower amphibolitic crust to generate more differentiated magmatic products. However, the dynamic coupling of the mechanisms leading to chemical differentiation and the formation of evolved magma during their ascent is still poorly understood (e.g., Jackson et al., 2003, 2005; Annen et al., 2006; Solano et al., 2012). This is mainly because the magmatic processes occurring at the base of the crust are difficult to grasp as they depend on complex thermal, physical and chemical interactions (e.g., Bouilhol et al., 2015).

The formation of upper crustal plutons requires that melts separate from their solid residue within lower crustal melt-bearing sources and ascend through the crust up to the root of the plutons on the order of 100 kyrs to 1 Myrs (e.g., Paterson & Tobisch, 1992; Shoene et al., 2012; Caricchi et al., 2014). External forces and physical properties of the melting rock control the mechanics of melt extraction, which can be driven either by dilatant structures during tectonic events, by buoyancy-driven porous melt migration (Bouilhol et al., 2015), diapirism (e.g., Paterson & Vernon, 1995; Miller & Paterson, 1999), or through a network of fractures (Brown &Rushmer, 1997). In the absence of externally applied stress, a silicate melt can only separate from residual crystals at low melt fraction by decompaction/compaction processes, in which the solid matrix deforms to expel the inter-granular liquid (McKenzie 1984, 1985). Partially molten material will compact only if the melt is interconnected, and if the density of the melt differs from that of the matrix (Wickham, 1987). Available evidence suggests that melt forms an interconnected network at melt fractions greater than 0.01, when the matrix grains are in textural equilibrium (von Bargen & Walf, 1986), or 0.02, when they are not in textural equilibrium (Wolf & Willy, 1991). This fraction is referred to variously as the melt connectivity or percolation threshold (e.g. Rosenberg and Handy 2005, Vigneresse et al. 1996; Petford 2003). At low melt fraction the rheology of the mixture is that of solid containing liquid along grain boundaries. The transition from melt at grain boundary to melt dominated transport occurs when the metrix becomes incoherent (Rosenberg & Handy, 2005; Connolly & Podladchikov, 2015), at a melt fraction ~ 0.4.

For mafic systems, the low viscosity of the melt (< 10^3 Pa.s) may lead to instabilities forming channels that propagate melt-filled porosity and leave behind trails of incompletely compacted porosity (Connolly & Podladchikov, 2007). These instabilities can manifest from the suprasolidus to the subsolidus crust, enabling melt to ascent (Bouilhol et al., 2011). For felsic systems, the efficiency of separation during compaction mainly depends on the melt viscosity and permeability of the solid matrix. Using typical values of granitic melt between 10^4 to 10^{11} Pas, Wickham (1987) showed that the compaction length was small, between 1 to 10m, and more importantly that the compaction time was of the order of 10^9 yrs. This shows that compaction alone is unlikely to drive segregation of large volume of felsic magmas over reasonable period of time (e.g., Rutter & Mecklenburgh, 2006). Several recent studies have shown, however, that melt transfer along grain boundaries is likely underestimated in the supersolidus continental crust. In the metapelitic migmatites of the El Oro Complex (Ecuador), Riel et al. (2016) used petrological, structural and geochemical studies to show that during biotite-breakdown reactions, melt was trapped and pervasively distributed in the garnet-bearing migmatite with evidence of meter-scale melt migration. In migmatitic orthogneiss from the Gföhl Unit (Bohemian Massif), Hasalová et al. (2008a) described 100-m scale pervasive flow from an external source produced migmatitic textures of high melt fraction. In the Ordovician Sierra Valle Fertil Complex of west-central Argentina, Walker et

al. (2015) studied an exposed lower crustal arc section. Based on petrological and geochemical studies, the authors show that the mafic section (mainly gabbronorites) was the locus of prolonged periods of (cyclic) magma injection, crystallization, and assimilation, with very efficient melt segregation at the kilometer scale. In the lower gabbroic crust of Fiordland (New Zealand), Stuart et al. (2016), using microstructural and in situ geochemical studies, showed that diffuse magma pathways were active at kilometer-scale. Moreover, the authors state that a rock at supersolidus conditions with minor incipient melt (< 5%) will be able to create a permeable, interconnect network allowing buoyancy-driven melt migration. As highlighted by Stuart et al. (2016), H_2O-rich externally sourced melt, injected inside the crust, decreases the melt viscosity by several orders of magnitude, thus allowing melt to be transported at grain-boundaries, through the lower crust, on realistic timescales (e.g., Jackson et al., 2003, 2005; Solano et al., 2012). Contrary to the crust, efficient porous reactive melt flow is well documented for ultramafic lithology (e.g., Dijkstra et al., 2003; Soustelle et al., 2009; Bouilhol et al., 2011). Interestingly, available geological examples of porous melt flow cover a large range of transport distances, from meter- to multi-kilometer scale. These distances show a clear scaling from felsic to ultramafic host-rocks (Fig. 1). Fracturing has also been proposed to be a likely mechanism enhancing melt segregation (e.g. Shaw, 1980; Petford, 1996). During fluid-absent partial melting, the buildup of compaction pressure promotes fracturing and vein formation at large fluid-overpressure tensile force of ~10 MPa (Petford, 1996). Apart from dyking, detailed studies of exhumed hot crustal zones have revealed alternative migration mechanisms characterized by mesoscale pervasive magma flow (Jagoutz et al., 2006; Bouilhol et al., 2015)(outcrop scale as opposed to porous flow): tectonic pumping, magma wedging in low viscosity rocks, and volatile-driven intrusion (Weinberg, 1999). Although porous flow and fracture-enhanced melt segregation are widely accepted mechanisms for the ascent of melt through the crust (Fig. 2), the transfer of melt through inter-granular network in the source region remains poorly studied. This is mainly because the system is complex as it depends on multiple physical parameters such as compaction pressure, temperature, composition, melting reaction, rheology, tectonic forces and inherited structures.

Nevertheless, geological, geochemical and geophysical evidence have shown that differentiation mainly occurs in the deep crust (e.g., Hildreth & Moorbath, 1988; Annen et al., 2006; Voss & Jokat, 2007), at suprasolidus conditions, where inter-granular melt flow is dominant (Fig. 2, zone III)(e.g. Jackson et al., 2003, 2005; Solano et al. 2012). At sub-solidus conditions, or at suprasolidus conditions when pervasive melt flow is assisted by fracturing, chemical interaction between melt and host-rock is likely to decrease, as magma ascent is focused in a mesoscale network of veins and dykelets (Fig. 2, zone II)(e.g., Weinberg, 1999). Below solidus conditions, the evolved magmas are localized in dykes, extracted toward higher structural levels and the melt/rock chemical interaction is low (Fig. 2, zone I)(e.g., Petford et al., 1993). During partial melting, the feedback between grain-boundary melt migration and heating of the host rock allows the solidus (Fig. 1) to reach increasingly shallower levels (Leitch & Weinberg, 2002). In turn this increases the thickness of the crust at suprasolidus conditions and favors magma differentiation, assimilation and hybridization.

Previous studies on the MASH zone coupling heat flow, two-phase flow and petrological modelling focused on parameterized reactive melt transport of partially melting crust (e.g., Jackson et al., 2003;2005; Solano et al., 2012); the relative contribution of partial melting of pre-existing crust and mantle-related magmas (e.g., Petford et al., 1993; Dufek & Bergantz, 2005), the thermal effect of multiple basaltic sill injection (Annen et al., 2006) and reactive melt transport coupled with binary phase diagram (Solano et al., 2014). Based on a parametric phase-modeling approach coupled with 1-D porous modeling, Jackson et al. (2005) showed that chemical interaction between melt and country rock during melt segregation has a

profound impact on the composition of the melt. From an initially homogeneous amphibolitic source rock they obtained a large diversity of melt composition, ranging from trondhjmetic to tonalitic, both spatially and temporally. Moreover, the authors showed that the melt composition is not only dependent on the initial composition, but is also controlled by the melt migration mechanism. Annen et al., (2006) used experimental data and numerical modeling to show that multiple emplacement of hydrous basalt sills at the base of the crust produces residual H_2O-rich melts with a strongly reduced melt viscosity, enhancing reactive melt flow at grain-boundary. Solano et al., (2012) used a similar approach to characterize the time required to form evolved magmas in the deep crust with the effects of residual hydrous-basalt melts. Using typical rate of emplacement for basalt in arcs (2-20 $mm.a^{-1}$), their modeling results indicate that chemical differentiation in the deep crust can occur by reactive melt flow along grain boundaries over timescale of 10 kyr to 1 Myr. More recently, Solano et al. (2014) used thermal and two-phase flow modeling coupled with binary phase diagrams, and showed that the evolution of a mush undergoing compaction produces variation of composition in both major and traces elements.

Previous studies allowed to model the first-order melt productivity and composition in a partially melting lower crust. However, parameterized phase-modeling can only be used in a restricted compositional domain (Bergantz & Dawes, 1994; Jackson et al., 2005). Although this approach allows capturing the importance of chemical interaction between ascending magma and the country rock (Jackson et al., 2003, 2005; Annen et al., 2006; Solano et al., 2012), the timescale of magma transport through the deep crust, and its chemical evolution, is likely biased as melt-assisted decompaction may enhance melt segregation to form channels (Connolly & Podladchikov, 2007). To further study the effect of chemical differentiation and crustal assimilation during mantle melt injection, partial melting and melt ascent in a deep mafic crust, we developed a thermo-mechanical two-phase flow code coupled with thermodynamic modeling via Perple_X (Connolly, 2005). Our approach allows modeling the physical and chemical effects of melt-assisted decompaction during magma ascent in the deep crust, at suprasolidus conditions. We apply our **S**torage, **T**ransfer, and H**y**bridization of comple**x** liquid/rock system (STyx) code on a case study of mantle-derived magmas injection within the lower amphibolitic crust. We track the chemical and physical evolution of both the host-rock and the magmatic products through space and time.

2. Methodology

2.1. Mathematical formulation

To model two-phase flow through a viscous porous matrix we use the formulation of Connolly and Podladchikov (2007). Assuming a small porosity limit ($\varphi << 1$), asymmetric viscous compaction/decompaction of the solid framework, incompressible fluid and solid, the governing equations of buoyant melt flow along grain boundary in an homogeneous and isotropic medium are given by the conservation of solid mass

$$\frac{\partial \varphi}{\partial t} = \frac{-P_c}{\zeta} \tag{1}$$

where φ is the porosity, t the time, P_c the compaction pressure and ζ is the bulk viscosity such that

$$\zeta = R\frac{\eta_s}{\varphi} \tag{2}$$

where η_s is the shear viscosity of the matrix and R is a Heaviside step function equal to 10^{-3} when $P_c > 0$ and is equal to 1 when $P_c \leq 0$. The form and values of R are assumptions made to emulate the effect of weakening at negative compaction pressure (Connolly and Podladchikov, 2007).

The conservation of total mass combined with Darcy's law is

$$P_c = \zeta \nabla . \left(\frac{k}{\eta_f} (\nabla P_c - \Delta \rho g \widehat{u_z}) \right) \tag{3}$$

where η_f is the fluid viscosity, k the permeability, $\Delta\rho$ the density contrast between fluid and solid, g the gravity and $\widehat{u_z}$ the unit vector. Permeability is expressed as

$$k = k_0 \varphi^n \tag{4}$$

where k_0 is the background value of the permeability and n the porosity exponent in the permeability function. For an unperturbed matrix, useful characteristic scales to describe the system are given by the compaction length

$$\delta_c = \sqrt{\frac{\zeta}{\eta_f} k_0 \varphi^n} \tag{5}$$

which is the length-scale over which pore fluids can move independently of compaction processes, the reference compaction pressure

$$P_{c_{ref}} = \delta_c \Delta \rho g \tag{6}$$

the reference fluid speed

$$v_0 = \frac{k_0}{\varphi_0 \eta_f} \Delta \rho g \tag{7}$$

and the compaction time-scale

$$t_0 = \frac{\delta_c}{v_0} \tag{8}$$

The heat transport equation is given by

$$\rho C p \frac{\partial T}{\partial t} = \kappa \nabla^2 T + \nabla . (\vec{q} T) \tag{9}$$

where κ is the thermal conductivity and T the temperature and $\vec{q}$ is the fluid flux expressed as.

$$\vec{q} = \left(\frac{k}{\eta_f} (\nabla P_c - \Delta \rho g \overrightarrow{u_z}) \right) \tag{10}$$

Chemical transport of specific component in the fluid is

$$\frac{\partial \varphi C_i}{\partial t} = -\nabla . (\vec{q} C_i) \tag{11}$$

where C_i is the concentration in wt% of component i. The advection of solid component due to compaction/decompaction is

$$\frac{\partial C_i}{\partial t} = -\nabla.(\overrightarrow{v_s} C_i) \quad (12)$$

where $\overrightarrow{v_s}$ is the solid velocity, and is calculated according to the Terzaghi's effective stress principle

$$\nabla.v_s = \frac{-P_c \varphi}{\zeta} \quad (13)$$

To avoid singularities in the zero-porosity endmember case we approximate the absence of melt by having a low background porosity $\varphi_0 = 10^{-3}$. The code is tested in numerical benchmarks for a solitary wave solution and for chemical advection, and results are given in Figures 3A and 3B.

2.2. Petrological calculations

To model stable phases and melt composition we combine our model with thermodynamic calculations using Perple_X (Connolly, 2005). Our model intends to manage a wide range of composition, as we need to be able to reproduce both the differentiation of hydrous mantle melts and the melting of amphibolite. As such we modified the melt model of White et al. (2001) in the NCFMASH system by applying a correction of Gibbs free energy of +6.0 kJ, a temperature dependency of -3.7 and a pressure dependency of -1.6, for the magnesian end-member foL, as well as a correction of Gibbs free energy of -64.0 kJ, a temperature dependency of 69.0 and a pressure dependency of -3.0 to the iron endmember faL. For the solids, we used the solid solutions of Newton et al. (1981) for plagioclase, Dale et al. (2000) for amphibole (with a correction on the Gibbs free energy of +25.0 kJ for the ferro-tremolite endmember), Jennings and Holland, (2015) for pyroxene and Holland & Powell (1998) for garnet, olivine, chlorite, chloritoid, and spinel.

Those corrections are applied to reproduce the topology, mineral and melt composition of mafic melting experiments at pressure ≥ 7 kbar and temperature up to 1200 °C and differentiation of hydrous mantle melts. Amphibolite melting is benchmarked against the experimental results of amphibolite hydrous partial melting of Qian and Hermann (2013) at pressures ranging from 10 to 15 kbar and temperatures ranging from 800 to 1050 °C. Absolute errors in melt composition between the experiments of Qian and Hermann (2013) and the models are shown in Figure 4. To ensure that the melt model can handle various melt compositions (46 to 80 SiO_2 wt%), we also tested it against amphibolite melting experimental data from Sen and Dunn (1994) at 15-20 kbar and 850 to 1025 °C, PatiñoDouce and Beard (1995) at 7-15 kbar and 875 to 1000 °C and 715-900 °C and Zhang et al. (2013) at 12 kbar and 800 to 1000 °C. Furthermore, to make sure that the model can account for the evolution of mantle derived melts, we have tested it against experiments of crystallizing hydrous-basalts of Müntener et al. (2001) at 12 kbar and 1025-1225 °C and Sisson et al. (2005) at 7 kbar and 800-950 °C, and show that our model reproduces fairly well the fractional crystallization of primary hydrous mantle melts in various pressure conditions. Figures S1 to S19 in the supplementary data illustrate the error estimates between experimental data and modeled compositions of melt and stable phases.

In the model, pressure, temperature and whole-rock composition are used to calculate the stable phases, including melt and their composition. First the heat equation is solved implicitly to calculate the temperature field. Then, he reaction energetics are taken into account by calculating the effect of latent heat of melting/crystallization as:

$$\Delta T = \Delta M \frac{\rho^{melt} H}{\rho^{mean} Cp^{mean}} \quad (14)$$

where ΔM is the variation of melt mass, ρ^{melt} and ρ^{mean} are the densities of the melt and of the whole-rock, respectively, His the latent heat of melting and Cp^{mean} the average whole-rock heat capacity. As latent heat changes temperature and thus ΔM, thermodynamic calculations are done within an iterative loop. We consider that convergence occurs when the residual ΔM between two iterations is $< 10^{-4}$.

The degree of thermodynamic disequilibrium between the solid and the melt, or melt:rock ratio, is a fundamental parameter to assess during magma transfer, as it controls fractional melting/crystallization and hence the chemical evolution of both melt and host-rock. Contrary to previous modeling studies using parametric petrological modeling (e.g., Jackson et al., 2003, 2005; Dufek & Bergantz, 2005), we take into account an effective melt:rock ratio (Fig. 5). We simplify the concept of thermodynamic equilibrium by assuming that 100% of the melt will be in thermodynamic equilibrium with a fixed weight fraction of the host-rock it travels through. So if, for example, the prescribed melt:rock ratio is 1:1 and there is 10 wt% of melt in a cell, the melt composition is equilibrated with an equal mass of the host-rock composition, which is henceforth referred to as the interaction zone. The remaining material (80 wt% of the total in this example) is referred to as host-rock. At the beginning of every timestep, the size of the interaction zone is adjusted. If the melt/interaction zone fraction is greater than the prescribed melt:rock ratio, a fraction from the composition of the host-rock is added to the interaction zone to match the prescribed melt:rock ratio. On the contrary, if the melt/interaction zone fraction is smaller than the prescribed melt:rock ratio, the composition of the excess interaction zone fraction is added to the host-rock. Whereas in nature the melt:rock ratio depends on multiple parameters such as permeability, velocity and the geometry of the interconnect melt network, in our model we simplify it to a constant value to be able to constrain its first order control on the system.

2.3. Modeling approach

Equations (1), (3), (9), (10) and (12) are solved with a finite volume discretization scheme using the Portable, Extensible Toolkit for Scientific Computation, PETSc (Balay et al., 2001).

First, equilibrium phases are calculated using Perple_X for every control volume, including the melt content and the composition of each stable phase. The effect of latent heat is taken into account using equation (14). Then, using the calculated melt content and the physical parameters presented in Table 1, we solve equations (1) and (3) through an iterative scheme: the implicit pressure solution obtained with Eq. (3) is inserted in Eq. (1) and solved explicitly to get an updated porosity. Using the updated porosity, pressure is solved again. Iterations between pressure and porosity solutions continues until the maximum relative pressure residue between two iterations is $<10^{-10}$. Subsequently, we solve Eqs. (10), (9) and (12) using an implicit method. When free water is present, melt and fluid are considered to behave as one fluid phase. Although this is a simplification, as free water and melt should be considered as a multiphase flow medium, in our simulations free water only occurs very episodically, either at the beginning or the end of the simulations, and is rapidly incorporated in melts and/or crystallized in water-bearing minerals.

3. Model setup of an application

As an example application, we investigate and quantify the role of the pre-existing crust in controlling the volume and composition of magmatic products during a magmatic

event affecting the lower crust: We consider the lowermost part of a pre-existing lower crust sitting atop of the mantle-wedge and subject to underplating of mantle-derived hydrous basalt (Fig. 6A). We present the results of three models to investigate the relative contribution between partial melting and fractional crystallization: a 'partial melting' model (PM) without injection of mantle-derived magma but with partial melting of the crust; a dynamic 'fractional crystallization' model (FC) of mantle-derived, injected melt travelling through the model without partial melting of or chemical interaction with, the host rock; and a 'reactive melt flow' model (RMF) combining both partial melting of the host rock and injection of mantle-derived melt.

Our model domain is 3 km thick discretized over a vertical 1-D regular mesh with 96 control volumes (Fig. 6A). Although, there is not much data (to our knowledge) on the actual thickness of the MASH zone, available studies suggest that it is most likely comprised between 1 and 10 km thick (e.g., Jackson et al., 2002; Walker et al., 2015). Jackson et al. (2002) showed that 2 km was enough to strongly influence the compositional evolution of the magmatic products segregated from the MASH zone. In this study we set our model thickness to be 3km. We are aware that varying this thickness may affect the system as it influences the temperature evolution of the top boundary, where magmatic products are extracted. However, investigating this parameter is beyond the scope of this paper and will be explored in future studies.

As boundary conditions, we assume open top and bottom boundary conditions for chemical advection of both host-rock and melt composition. This implies that mass conservation is ensured when $\Delta\varphi \neq 0$, by chemical advection of the host-rock.

Lithostatic pressure at the top boundary is set to be $P_0 = 0.9$ GPa (~30 km) to reproduce the conditions in the deep hot crust of exposed oceanic volcanic arcs. Then for each control volume the lithostatic pressure (P_i) is calculated from top to bottom using densities obtained with Perple_X as

$$P_i = P_{i-1} + \rho_i g \Delta z \quad (15)$$

where P_i is the lithostatic pressure in the i^{th} control volume, Δz is the control volume size in the vertical direction and ρ_i is the average density of the melt-rock mix in the i^{th} control volume.

For the fluid flow $\nabla P_c = -0.1$ Pa.m^{-1} at the top boundary condition. We simplify the emplacement of the hydrous-basalt magma at the bottom boundary as being constantly injected at a rate $\vec{q}_{basalt}$ = 4mm.yr^{-1}, corresponding to a typical time-averaged magma productivity in arc setting (Crisp, 1984). This results in progressive heating of the lower crust from subsolidus to suprasolidus conditions, hence creating a new MASH zone. Simultaneously, the crystallizing hydrous-basalt at Moho temperature generates fractionated melt, which ascends through the MASH zone. To simulate fractionated melt injection at the Moho within the overlying crust, we use an influx boundary condition at the bottom such that:

$$\vec{q}_{influx} = \vec{q}_{basalt} F_{melt} \quad (17)$$

where $\vec{q}_{influx}$ is the influx of fractionated melt from crystallizing basalt, $\vec{q}_{basalt}$ is the rate of basalt emplacement at the Moho and F_{melt} is the parametrized fraction of fractionated melt as a function of temperature (after Sisson et al., 2005 and Müntener et al., 2001).

Within the model, the initial temperature profile is set to vary linearly with a gradient of 20 °C.km^{-1} reaching a temperature of 600 °C at the bottom boundary (Fig. 6B). On the top

boundary $\nabla T = 0.02$ K.m^{-1}. On the bottom boundary, temperature is then prescribed to be time-dependent in order to simulate the thermal evolution of the Moho during multiple basalt magma emplacements (Fig. 6C). The bottom temperature boundary condition T_b is time-dependent and is of the form

$$T_b = C_1 + C_2 \log(t) + C_3 \frac{t}{t_{max}} \sin\left(\frac{t}{t_{max}}\right) \quad (18)$$

where t is time in years, t_{max} 4.5 × 10^6 years and C_1, C_2 and C_3 are constants. The temperature at the bottom progressively increases up to 1140 °C at 2.5 Myr, and is set to remain constant during 0.5 Myr between 2.5 and 3.0 Myr before cooling down to 4.5 Myr.

As starting material for the mafic lower crust we use the amphibolite composition "Mix-B" of Qian and Hermann (2013) in the NCFMASH system. On the bottom boundary, the composition of the injected melt that fractionated from the underplated, crystallizing basalt is parameterized following Annen et al. (2006), using polynomial fits (see Figure 7). For low temperatures (< 1075 °C) we use the 0.7 GPa experiments of Sisson et al. (2005)on a Cascades basalt (sample 87S35A) with 2.3 wt% H_2O. For high temperatures (> 1075 °C) we use the 1.2 GPa experimental data of Müntener et al. (2001) for a Cascades basaltic andesite (sample 85-44) with initial H_2O content of 3.8 wt%. We assume that the mantle-derived magmas are emplaced below the Moho and that the composition of the injected melt(is solely controlled by the temperature at the Moho. The coefficients of the polynomial regressions used to parameterize the composition of mantle-derived melt are presented in Table 3. Although we do not take into account K_2O in the thermodynamic calculations, it is injected in the model and advected as a passive component. Therefore, we assume that the K_2O-content of the melt is only controlled by the mantle-derived melt.

Resolution tests have been performed using the reactive melt flow model setup presented in §4.3. We used 24, 48, 96 and 192 control volumes to study the effect of the spatial resolution on the evolution of the phase proportions, their composition and the extraction rate. Results at the top boundary of the model, where melt is extracted, are presented in Figure 3c-g. Models with resolutions of 24 and 48 exhibit slight differences in phase proportions compared to models with higher resolution of 96 and 192 (Fig. 3c). When looking at the melt extraction rate and its SiO_2 and H_2O contents, only the lowest resolution model of 24 exhibits significant deviation with to the other tested resolutions (Fig. d-g). Overall, variations of modeled phase proportion, extraction rate and composition are only observed for the low resolution models of 24 and 48 while higher resolution of 96 and 192 exhibit nearly identical results. Consequently, we select the optimal spatial resolution for our model to be 96.

4. Results

4.1. Partial melting model (PM)

This model corresponds to an end-member in which the crust partially melts as a response of a thermal anomaly, without any injection of mantle-derived magmas. This allows quantifying the melt composition and productivity of a partially melting amphibolitic crust. By comparison with models in which injection at the Moho is taken into account, it will help us to quantify the relative contribution between crust and mantle-derived melts in the genesis of felsic crust. This model is achieved using a melt:rock ratio of 1:1 and the results are presented in Figures 8, 9 and 10.

The starting mineral assemblage is composed of 53.66 % of amphibole, 11.5 % of garnet, 17.7 % of plagioclase and 16.4 % of quartz (Fig. 8A). As the model heats up, the solidus of

the amphibolite is crossed at the bottom boundary after 0.23 Myr at 760 °C (Fig. 8). Subsequently, the solidus propagates upward, the first melts are collected to generate porosity waves containing up to 2 wt% of melt, and after 0.55 Myr the first wave reaches the top boundary (Fig. 8B). The first melt batch is produced via quartz consumption together with amphibole, at about 30-31 km, and just deeper, where the temperature exceed 850°C (Fig. 8B), (31-33 km depth), orthopyroxene appears as a peritectic product of this melting reaction. Meanwhile in the host rock, garnet and quartz are consumed to produce orthopyroxene.. At the bottom boundary, where quartz is fully consumed, and the temperature > 910°C, the model show the appearance of peritectic clinopyroxene produced by amphibole-breakdown melting reaction(Fig. 8B). As temperature continues to rise, it takes approximately 0.7 Myr (from 0.6 to 1.3 Myr) for the clinopyroxene-in reaction to reach the top of the modeled region (Fig. 8B,C,D) leaving behind a crust devoid of amphibole and made of gabbronorite. Figure 8C,D show that a large bulge of melt accumulates below the clinopyroxene-in reaction, reaching up to 15 wt% of melt at 1.2 Myr and right before reaching the top of the model. The fact that this bulge accumulates melt instead of being propagated as smaller porosity waves is related to a jump in the melt composition. This is expressed in figure 9F where extracted melt prior 1.3 Myr is SiO_2-rich (>72 wt%) while its SiO_2-content decreases down to < 60 wt% after.

In Figure 9 we present the evolution of the rate of emplacement, cumulative thickness and composition of the extracted melt in time. The first extracted melt is hydrous and silica-rich and has an anhydrous composition of SiO_2 = 76.5 %, Na_2O = 5.0 %, CaO = 2.9 %, FeO = 1.3 %, MgO = 0.7 % and Al_2O_3 = 14.0 % (Fig. 9). From 0.55 to 1.4 Myr, amphibole breakdown drives partial melting and produces up to 460 m of felsic products with: nearly constant Na_2O-, Al_2O3-, CaO- and SiO_2-contents, increasing MgO-content from 0.7 to 1.3%, FeO-content from 1.3 to 3.1%, and decreasing H_2O-content from 12.5 to 7.0%. During this period, the average rate of emplacement is of ~0.5 $mm.yr^{-1}$ with four main peaks of activity at 0.61, 0.75, 0.89 and 1.32 Myr, reaching a maximum rate of emplacement of 0.9 $mm.yr^{-1}$ (Fig. 9). At 1.6 Myr, amphibole is almost consumed (Fig. 8) and the remaining melt equilibrates with an anhydrous host-rock made of orthopyroxene, plagioclase and clinopyroxene. Between 1.6 and 1.8 Myr, the last melts that are extracted exhibit increasingly intermediate compositions. The (anhydrous) composition of the extracted last drop of melt is SiO_2 = 55.0 wt%, Na_2O = 5.9 wt%, CaO = 4.7 wt%, FeO = 11.6 wt%, MgO = 5.2 wt%, Al_2O_3 = 18.8 wt%. Although the temperature still rises up until 2.4 Myr, the system is anhydrous and does not melt any further. In total, nearly 460 m of felsic magma are extracted in 1.1 Myr (Fig. 9).

For the PM model, the molar Mg# (Mg/(Mg+Fe)) of the extracted melt remains nearly constant at 38 between 76 and 73 wt% of SiO_2 and slightly increases to 43 as the SiO_2-content decreases from SiO_2 = 76.5 down to 55 wt% (Fig. 10).

4.2. Dynamic fractional crystallization model (FC)

To quantify the role of mantle-derived melt in the genesis of the magmatic products, we produced a model in which we only consider fractionation of mantle-derived melt. In this model, the primitive melt is injected at the bottom (following the parameterization presented in §3 and Fig. 7) and is undergoing fractional crystallization that forms cumulates and changes the melt composition, but is forced not to interact with the surrounding crust (Figs 9 to 12), and as such represent the opposite scenario of the PM model previously presented.

As temperature increases within the crust, at 0.3 Myr the first mantle-derived melt are stable in the lowermost part of the modeled section (Fig. 11A). At 0.6 Myr, the first porosity wave is generated and its ascent is controlled by thermal diffusivity. Because, thermal

diffusivity propagates the solidus at a slower rate than melt flow, the first melt wave accumulate a large fraction of melt (Fig. 11B), which reach the surface at ca. 1 Myr. Between 0.3 and 1.0 Myr, the characteristic cumulate mineral assemblage recorded at the bottom boundary is made of garnet + plagioclase ± amphibole (Fig. 11D). At 1.0 Myr, the first extracted has a felsic composition: SiO_2 = 68.7 %, Na_2O = 5.9 %, CaO = 3.8 %, FeO = 3.8 %, MgO = 1.2 %, Al_2O_3 = 17.2 % (Fig. 9). Between 1 and 2 Myr the extracted melt composition quickly becomes intermediate and reach its lowest SiO_2-content of ~ 52.5 wt%. This goes along with crystallization of cumulate assemblage composed of clinopyroxene + plagioclase (Fig. 11D). Meanwhile the steady-state propagation of porosity waves is established (Fig. 11C). After 2.4 Myr, the temperature decreases and the SiO_2-content rises again and reach 75.6 wt% at 4.5 Myr. The compositional variations between injected and extracted melt are mainly related to the crystallization of garnet, plagioclase ± amphibole ± quartz at temperature < 1000 °C, while it is controlled by the crystallization of clinopyroxene ± plagioclase at higher temperature (Fig. 11D). The rate of melt extraction is similar to the rate of injection during most of the simulation with the one exception at ~ 1 Myr, where it forms a high peak of 2.3 $mm.yr^{-1}$ (Fig. 9I). This peak is related to the accumulation of melt during the ascent of the solidus during the first stage of the model (< 1.0 Myr).

During the heating phase (0-2 Myr), the Mg# of the extracted melt increases from 32 to 53 while the SiO_2-content decreases from 68.7 to 52.5 wt% (Fig. 10). During the cooling phase (2.5-4.5 Myr) the trend is similar with a minimum Mg# of 23 for a SiO_2-content of 76.5 wt%. However, we note a slight increase of the Mg# to 33, between 66.5 and 70.0 SiO_2wt%.

For the dynamic fractional crystallization model, a total of 7080 meters of products are extracted (Fig. 9), with a large proportion having an intermediate composition (SiO_2 < 63 wt%). In the QAP diagram (Streckeisen, 1976), these products exhibit a trend from granodiorite (SiO_2 > 70 wt%) to diorite/gabbro (SiO_2 ~ 53 wt%), passing through the quartz-monzonite and monzonite fields (Fig. 12). **4.3. Reactive melt flow model (RMF)**

In this model we combine both injection of mantle-derived melt and interaction with the amphibolitic host-rock. This model is achieved using a melt:rock ratio of 1:1 and the results are presented in figures 9, 10, 12, 13 and 14.

Similarly to PM model, the starting composition is made of 53.66 % of amphibole, 11.5 % of garnet, 17.7 % of plagioclase and 16.4 % of quartz (Fig. 13). At 0.3 Myr temperature below 760 °C, the mantle-derived melt is not yet stable within the amphibolitic host crystallizing at Moho depth, releasing water that is transferred upward, forming a porosity wave (Fig. 13A). This water-filled porosity wave is followed, at 32-33 km depth, by a first mantle-derived melt wave (Fig. 13A). The first melt is extracted at 0.35 Myr and has a felsic composition: SiO_2 = 77.0 wt%, Na_2O = 5.6 wt%, CaO = 2.2 wt%, FeO = 3.8 wt%, MgO = 1.2 wt%, Al_2O_3 = 13.5 wt% (Fig. 9). As temperatures rises between 0.3 and 0.6 Myr, multiple melt-filled porosity waves composed of a mixed of injected mantle-derived and in situ partial melt are ascending through the modeled region (Fig. 13B). From 0.35 to 1.3 Myr the composition of extracted melt remains felsic (SiO_2> 63 wt%). During this period the FeO-, MgO-, CaO-, Na_2O- and Al_2O_3-contents increase to 4.0, 1.5, 3.0, 6.0 and 17 wt%, respectively (Fig. 9). The SiO_2- and H_2O-contents decrease to 68.0 and 9.0 wt%, respectively. Partial melting occurs in the same fashion as for the PM model where amphibole and quartz produce melts, then melt and orthopyroxene, while the host rock shows the appearance of orthopyroxene at the expense of garnet and quartz. Hornblende is disappearing to form melt and clinopyroxene once quartz in consumed. After 1.4 Myr the amphibole is largely consumed and the extracted melt reach their minimum SiO_2-content of ~53 wt% at 1.8-1.9

Myr (Fig. 9). Meanwhile the MgO-content in the extracted melt increases to 5.5 wt%, the FeO-content to 10.0 wt%, the CaO-content to 6.0 wt% and the Al_2O_3-content to 20.0 wt%, while the H_2O-content decreases to 7.0 wt% and the Na_2O-content to 4.8 wt% (Fig. 9). During the same period melt-filled porosity waves represent a mix of mantle-derived melt and in situ partial melting controlled by the peritectic crystallization of clinopyroxene (Fig. 13C). For instance at 1.8 Myr, as much as five porosity waves can be identified rising through the modeled region (Fig. 13C). From 3.0 to 4.5 Myr the composition of extracted melts progressively become felsic again and largely follow the trend of the dynamic fractionation model, with slightly higher MgO-content and lower Na_2O-content (Fig. 9). At temperatures lower than 850 °C, in the interaction zone, the melt is in equilibrium with amphibole + plagioclase + quartz + garnet, while the host rock is characterized by the assemblage plagioclase + clinopyroxene + orthopyroxene (Fig. 13). At temperature greater than 850 °C the melt is in equilibrium with plagioclase + clinopyroxene ± garnet, while the host rock is characterized by the assemblage made of plagioclase + clinopyroxene + garnet with minor orthopyroxene (Fig. 13).

The Mg# in the melt shows a relatively complex relationship relative to SiO_2, with asymmetric heating/cooling phases (Fig. 10). During the heating phase, between 0 and 2.4 Myr, the Mg# first exhibits nearly constant values around 37-38 with decreasing SiO_2-content from 77 to 67.5 wt%. Then, from SiO_2 = 67.5 to 60.0 wt% the Mg# increases between 38 and 45. From SiO_2 = 60.0 to 53.0 wt%, the Mg# linearly increases from 40 to 51, similarly to the dynamic fractional crystallization model (Fig. 10). During the cooling phase, the Mg# trend deviates from the dynamic fractional crystallization model at SiO_2-content > 60.0 wt%, and oscillates untilSiO_2 = 75.0 wt%. These Mg# oscillations have a mean amplitude of 5 following a general tendency of decreasing the average Mg# from 40 down to 32 with increasing SiO_2-content from 60 to 70.0 wt%, and increasing it again from 32 to 38 with increasing SiO_2-content from 70 to 75.0 wt%. In the QAP diagram (Fig. 12) the extracted products follow the trend of the fractionation model melt during the cooling phase. However, during the heating phase, they trend from granodiorite to diorite/gabbro field going through quartz-diorite/quartz-gabbro field (Fig. 12).

Overall, a total of 7600 m of products is extracted from this model, with a quarter of the total volume having a felsic composition and the rest having an intermediate composition. Figure 14 presents the relationship between rate of extraction, cumulative extracted thickness and mantle proportion in the extracted product. The overall crustal contribution is of ~18 % (Fig. 14c). This crustal contribution is mainly expressed during the heating phase with a mean value of 25%, while the cooling phase is almost entirely controlled by the mantle-derived melt with a mean crustal contribution < 5 % (Fig. 14).

5. Discussion

5.1 Role of pre-existing crust

Our results further support that partial melting due to a thermal anomaly cannot be a viable mechanism to generate large amount felsic to intermediate magmas forming the mid-to upper crust (Fig. 9). The volume of products generated during dynamic partial melting of a 3km thick amphibolite is limited ~ 460m (Fig. 9J). Moreover, the composition of extracted partial melt shows a very narrow range of composition with a SiO_2-content of 73 to 77 % and a nearly constant Mg# of 37-40. This is because during partial melting only, water is not renewed which precludes any further melting (Fig. 8). Consequently, the system becomes anhydrous and the solidus is shifted to a higher temperature. Instead, the results of the dynamic fractional crystallization model indicate that emplacement of mantle-derived melt at

Moho level is able to generate a large volume (7080 m) of felsic to intermediate products (SiO_2 53-77 wt%). However, among these 7080 m of extracted products only 5.7% is felsic while 94.3% is intermediate.

The RMF model couples both partial melting processes of pre-existing amphibolitic crust and injection of mantle-derived melt, and produces a slightly larger volume of melt (7600 m), and a similar range of felsic to intermediate products (Fig. 12). However, the extracted products are more felsic (22.7%) and less intermediate (78.3%) than for the fractional crystallization model. By adding up the products of partial melting and dynamic fractional crystallization modeling, we could suggest that the pre-existing crust contributes to 5.3% of the total extracted products. However, Figure 14 shows that for the reactive flow model the extracted products have an average of 16% from crust contribution. This indicates that reactive melt flow of mantle-derived melt through an amphibolitic crust further enhances its productivity. We quantify that 1200 m of the total 7600 m of extracted products from the RMF model is generated by the crust. This implies that 40% of the pre-existing amphibolitic crust has been refined to produce the new felsic to intermediate crust. The interaction between mantle-derived melt and the crust host-rock is also marked by the progressive enrichment of mantle-derived material in the crust reaching up to 35% by the end of the experiment (Fig. 14). Overall, we find that the mantle contributes up to 84% of the total extracted products and contribute to ~70% of the felsic component. These values are comparable with oxygen isotope study on continental arc granitoids which show a significant (>80%) contribution of the mantle to continental arc granitoids (Kemp et al., 2007). Our results also indicate that during a magmatic event affecting the lower arc crust, the contribution of pre-existing hydrated amphibolitic crust is significantly higher than when steady-state high-temperature geotherm is established (Fig. 14). Finally, the results of the RMF model show that the integrated composition of the extracted magmatic products, although crossing the andesitic composition, is widespread and cannot explain the large volume of exposed andesite (Fig. 9)(Reubi & Blundy, 2009). This is coherent with recent studies showing that shallow mixing and mingling between felsic and intermediate melt is required to generate Andesitic magmas (Reubi & Blundy, 2009).

5.2. Applicability, limitations and future developments

The application presented here highlights the knowledge that can be gained by using a numerical approach that couples two-phase flow, heat flow and petrological calculations. It allowed us to study the first order role and contribution of mantle-derived magma over partial melting or pre-existing amphibolitic crust in the differentiation of the magmatic products segregated from the MASH zone.

However, the control of boundary conditions and other physical parameters on the modelling results is yet to be investigated. For instance, here we assume a constant influx of mantle-derived melt at Moho level and a negative compaction pressure gradient at the top boundary to facilitate melt extraction. Although this allows modelling the compositional evolution of both melt and host-rock during deep crust magma transfer, different boundary conditions will likely influence the compositional evolution of the system. Indeed, influx of mantle-derived magma into the lower crust is known to occur through multiple sill emplacement (e.g., Annen et al., 2006; Solano et al., 2012), which may evolve to feeder pipes as observed in arc lower crustal sections (Bouilhol et al. 2015), while melt extraction to shallower levels of the crust is known to be controlled by the transition of grain-boundary- to dyke-dominated melt transport (e.g., Weinberg, 1999). The dynamics of mantle-derived melt injection and the processes of melt extraction at the top of the suprasolidus crustal region may therefore affect the

temperature evolution, the melt content and distribution, and the overall compositional evolution of the system. Other parameters such as permeability, composition-dependent melt viscosity, lithostatic pressure, asymmetric factor of compaction/decompaction, thickness of the modelled suprasolidus region, chemical heterogeneities of the starting material and multi-dimensional effects of melt migration will also control the dynamics of the MASH zone and impact the modelling results. An extensive parametric investigation of the role of each parameter is beyond the scope of this paper, and we leave it to future studies will have to address the modeling sensitivity.

Although the application presented in this study focuses on lowermost crust magmatic processes, our modeling approach is valid for other fluid/rock systems. As long as a relevant thermodynamic database is given, our new approach allows to model fluid/melt transfer through a rock medium. For instance, our approach can be applied for mantle conditions to study partial melting of peridotite and the chemical evolution of those melt as they ascend through the mantle. However, several limitations of our numerical approach must be highlighted. First, solid deformation due to tectonic forces is not yet taken into account, our approach cannot be applied when tectonic deformation is thought to play a major role in controlling fluid/rock dynamics. Secondly, our approach cannot be applied for systems where dyking becomes the main mechanism of fluid/melt transfer. Indeed, dyking and related fluid/melt transfer constitutes an even more complex system, where elasticity and mechanical deformation has to be taken into account (e.g., Keller et al., 2013). Thermodynamic disequilibrium between the fluid/melt and the host-rock is also not yet taken into account in our approach. While the melt does not have to be in chemical equilibrium with the whole-rock composition, we assume that the melt is always fully in equilibrium with the pressure and temperature conditions of the cell it belongs to. Although this is likely valid in the lowermost crust of arc systems where melt transfer occurs at suprasolidus conditions at grain-boundary (e.g., Annen et al., 2006), it is likely wrong at temperatures lower or equal to the solidus (e.g., Weinberg, 1999). Finally, kinetics of reaction is one of the less constrained aspect concerning reactive transport of magma. In this study we assume that in the interaction zone petrological equilibrium is achieved every 1 kyr. Although, it is believed that for suprasolidus conditions the kinetics of reaction is fast (e.g., Agosta-Vigil et al., 2006), it is unlikely to be a constant in nature as melt fraction, water-content and segregation rate play important roles.

Acknowledgements

This study was supported by the European Research Council (ERC StG 279828). We also would like to thank Philippe Goncalves and one anonymous reviewer for their comments and suggestions that improved the manuscript.

FIGURES

Figure 1. Observed porous transport distance against rock/melt viscosity contrast. Observed porous transport distance after (1) Riel et al. (2016), (2) Hasalová et al. (2008a), (3) Stuart et al. (2016) and (4) Bouilhol et al. (2011). Mean melt viscosities at relevant temperature of interest are 10^5, 10^4, 10^3 and 10^1Pa.s for metapelite, orthogneiss (e.g., Scaillet et al., 1996), gabbro (e.g., Jackson et al., 2003) and dunite protoliths (e.g., Connolly and Podladchikov, 2007), respectively. Mean host-rock viscosities at the melt's temperature of interest are of the order of 10^{13}, 10^{16}, 10^{19} and 10^{19} Pa.s for metapelite (e.g., Hashim et al., 2013), orthogneiss, gabbro (Jackson et al., 2003) and dunite host-rock (Connolly and Podladchikov, 2007), respectively.

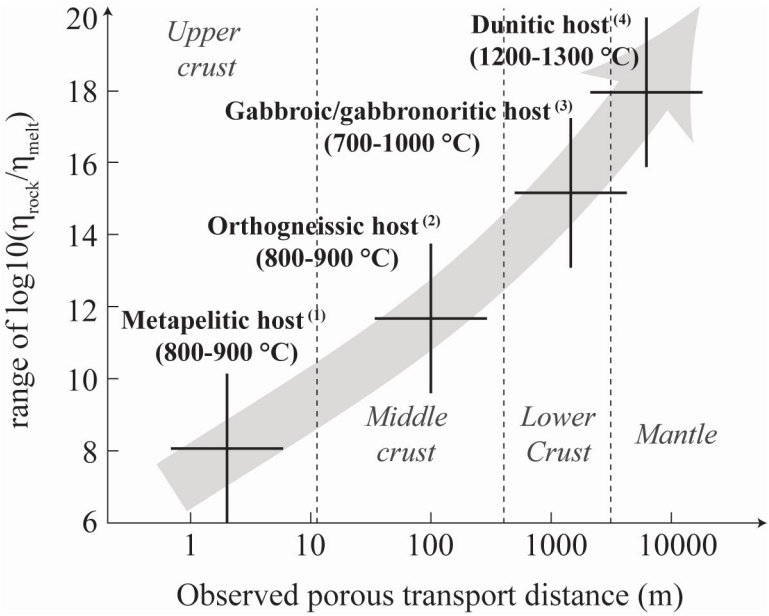

Figure 2. Schematic diagram of melt extraction mechanisms in a deep crust under static condition. Zone I, network of dykes feeding the main magma conduit to the pluton. Zone II, mesoscale network of veins and dykelets at subsolidus conditions. Zone III, inter-granular pervasive melt flow zone at suprasolidus conditions. Heat and melt injection at the bottom boundary of the diagram are related to the emplacement of mantle-derived magmas at Moho depth.

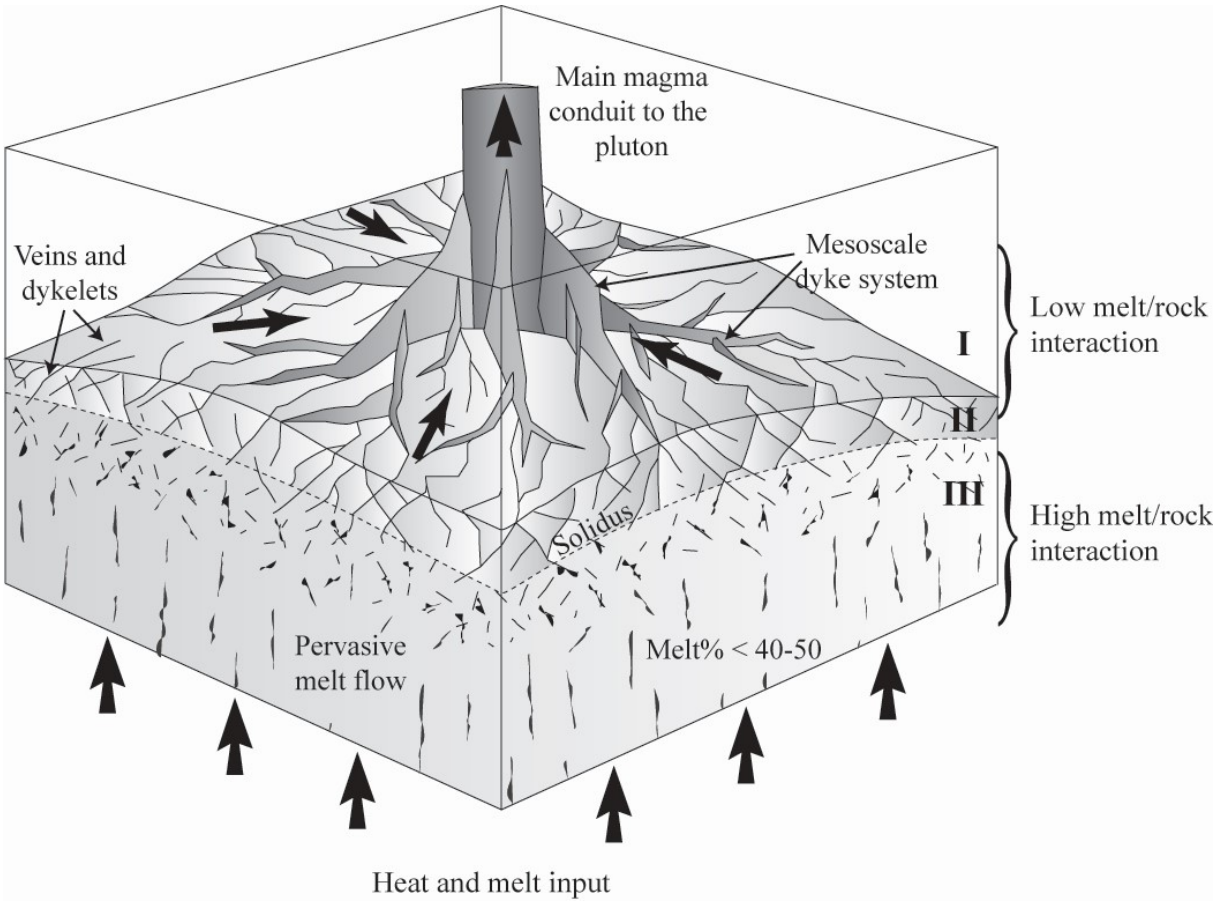

Figure 3. Benchmarks and resolution tests. A, Solitary wave benchmark. In black is the numerical solution from our code and red the analytical solution from Richard et al. (2012). Used parameters are n = 3, m = 1, $\phi = 10^{-3}$, $k_0 = 10^{-7}$ Pa.s, $\eta_f = 0.1$ Pa.s, $s = 10^{18}$, $\Delta\rho = 500$ kg.m^{-3}. B, Chemical advection benchmark. Benchmark has been achieved using three different resolutions. Benchmark starts with a step content from 1 to 0, and the composition is advected with time. Used parameters are n = 3, m = 1, $\phi = 10^{-2}$, $k_0 = 10^{-6}$ Pa.s, $\eta_f = 10^{3}$ Pa.s, $s = 10^{19}$, $\Delta\rho = 800$ kg.m^{-3}. C-F, Resolution tests on the evolution of the mode (wt%), extraction rate (D), cumulative thickness (E), SiO_2-content of extracted melt (F) and H_2O-content of extracted melt (G). The models have been run using the Reactive Melt Flow (RFM) setup using 24, 48, 96 and 192 control volumes. The plotted results are recorded at the top boundary of the models during their whole (4.5 Myr).

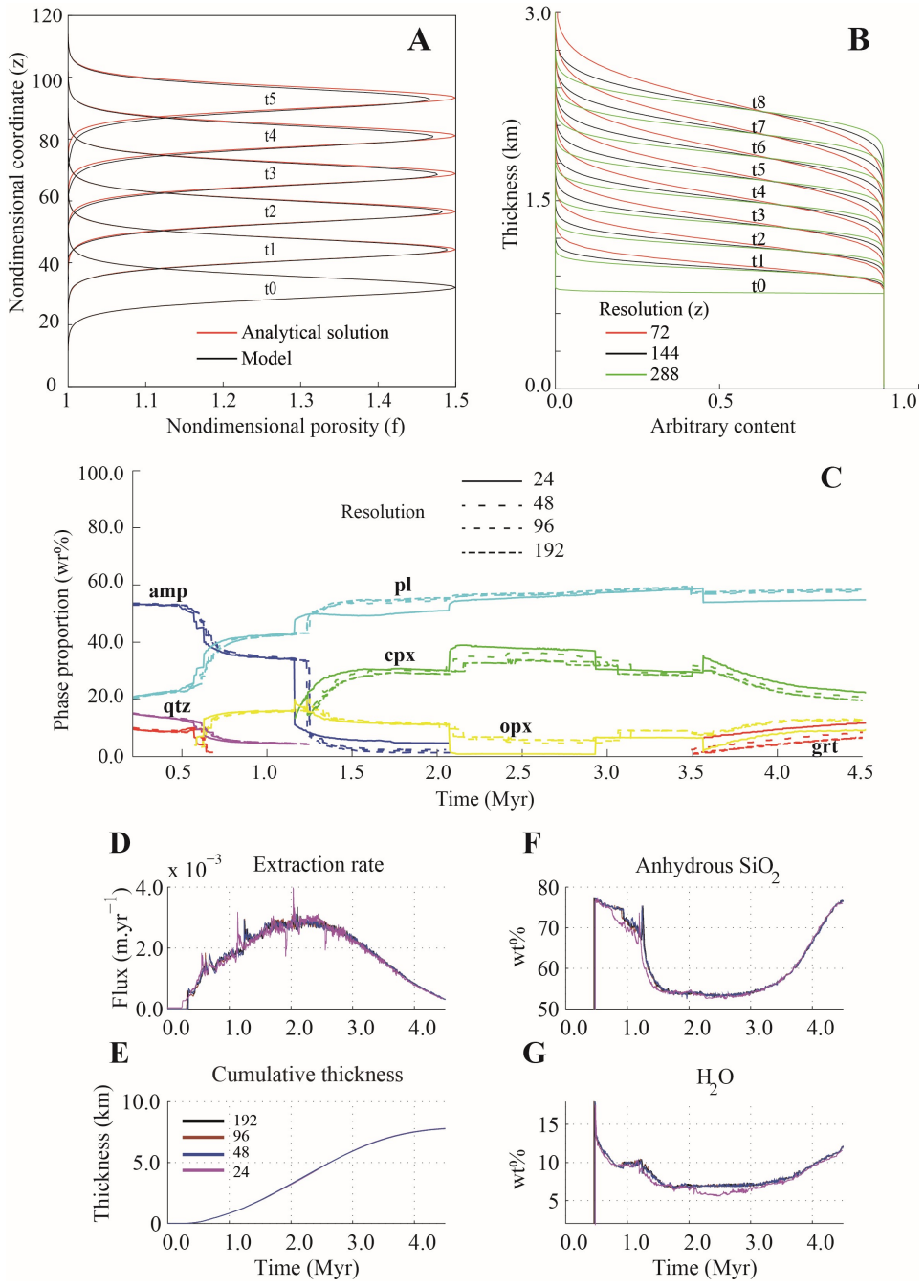

Figure 4. P-T relative error maps between experimental data and modeled melt composition. The starting composition is the MIX-B amphibolite sample of Qian and Hermann (2013) which is presented in Table 2. The heavy black dots show the P-T points where experimental data have been acquired by Qian and Hermann (2013). Error map for each oxyde X is calculated as $X^{modeled}$ - $X^{experiment}$.

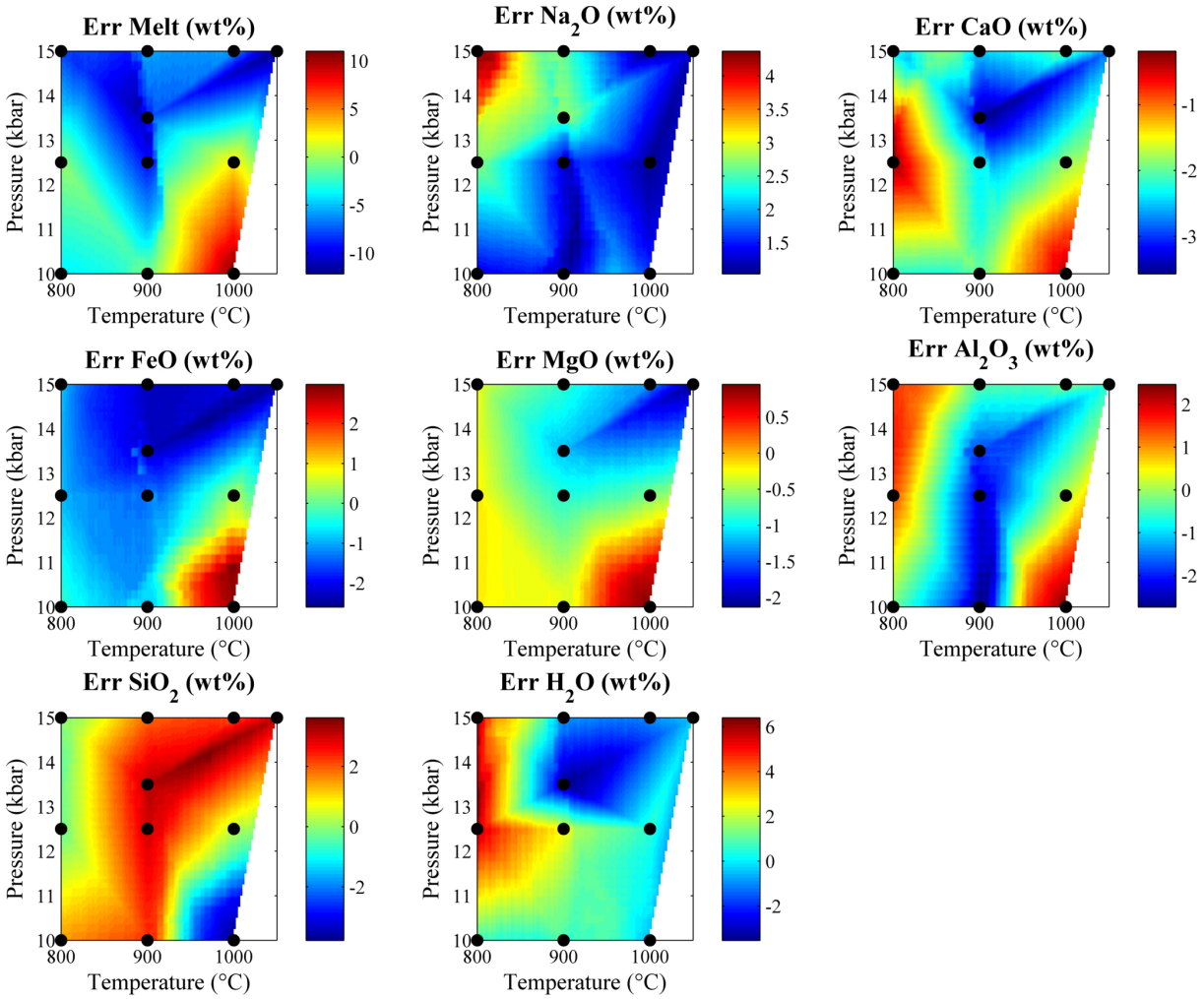

Figure 5. Porous flow and effective melt:rock ratio. The solid matrix decompacts when melt flows through it. The melt:rock ratio represents the fraction of solid which reacts with the melt and is considered in thermodynamic equilibrium with it. We call the solid fraction in equilibrium with the melt interaction zone (IZ) and the remaining solid the host-rock.

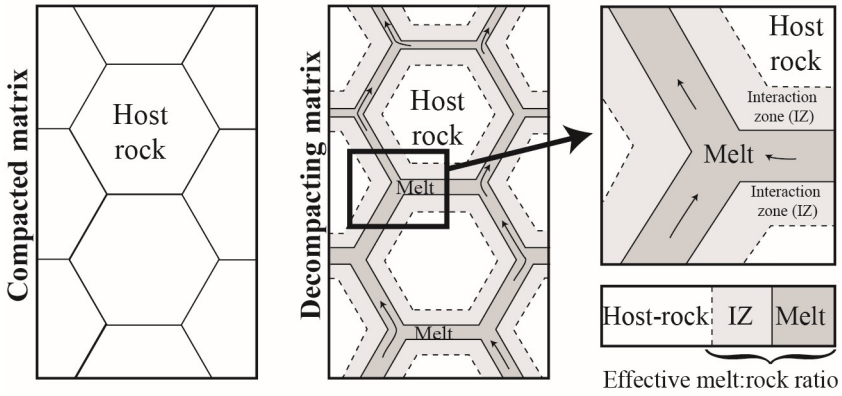

Figure 6. Model setup. A, Schematic representation of the modeled region. Fractionated melt from crystallizing mantle melts are injected at the bottom boundary, while extracted melts segregated from the crust are captured at the top boundary. B, Initial temperature profile. C, Time-dependent temperature bottom boundary condition. Note that temperature is maintained constant between ~2 and 2.5 Myr in order to reach a steady state. Then the temperature slowly decreases down to 4.5 Myr. During the cooling phase, the rate of mantle-derived magma emplacement is progressively decreased to 0.

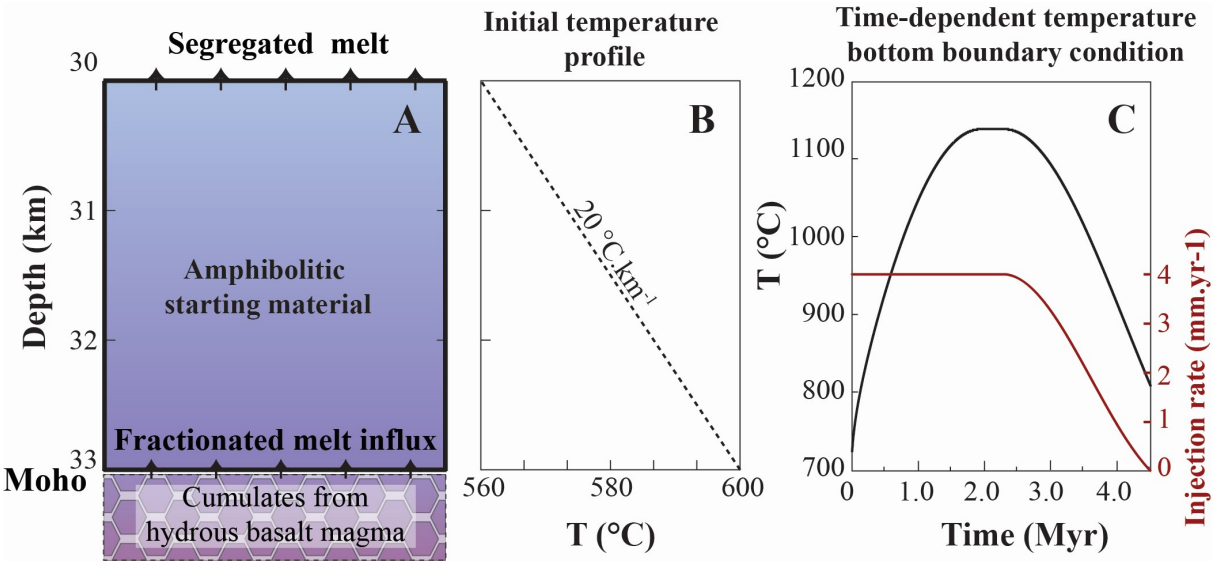

Figure 7. Parameterized composition of fractionating parental mantle melts injected at the base of the models. The white circles are from the experimental data of Müntener et al. (2001) at high temperature, while the grey circles are from the experimental data of Sisson et al. (2005) at lower temperature. Fits are achieved using high degree polynomial functions (see Table 3).

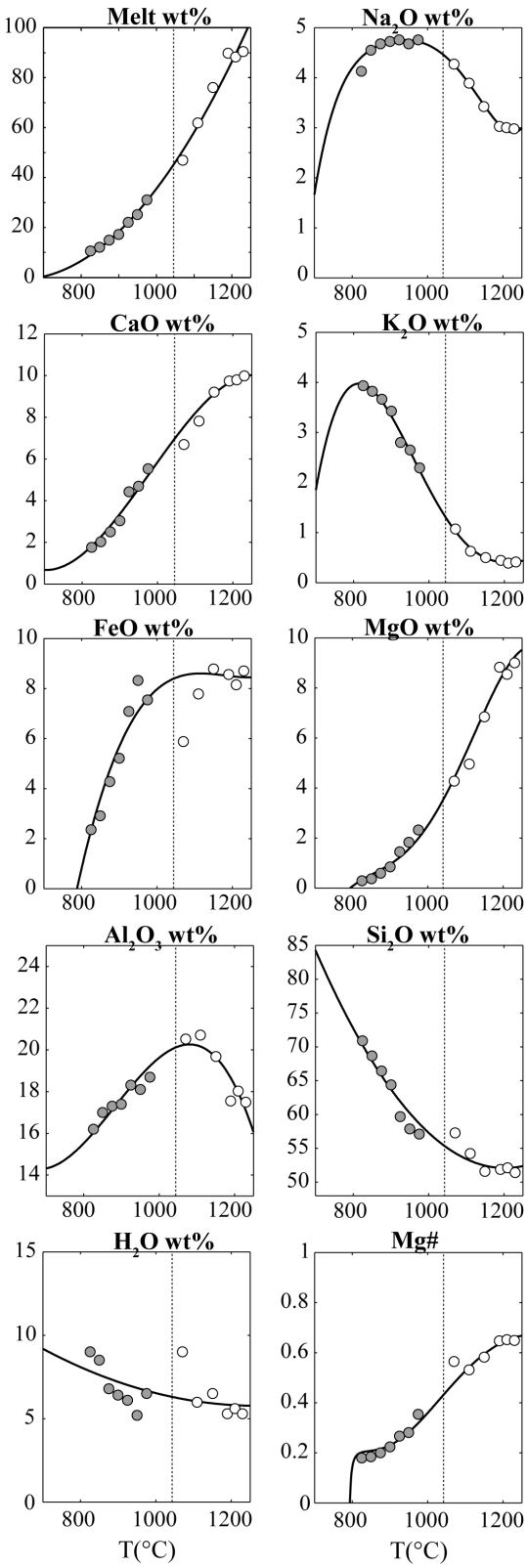

Figure 8. Stable phase evolution of the Partial Melting model. For each subfigure the left panel presents the temperature profile across the modeled section, the central panel shows the stable phases in the whole-rock and the right panel shows the stable phases in the interaction zone.

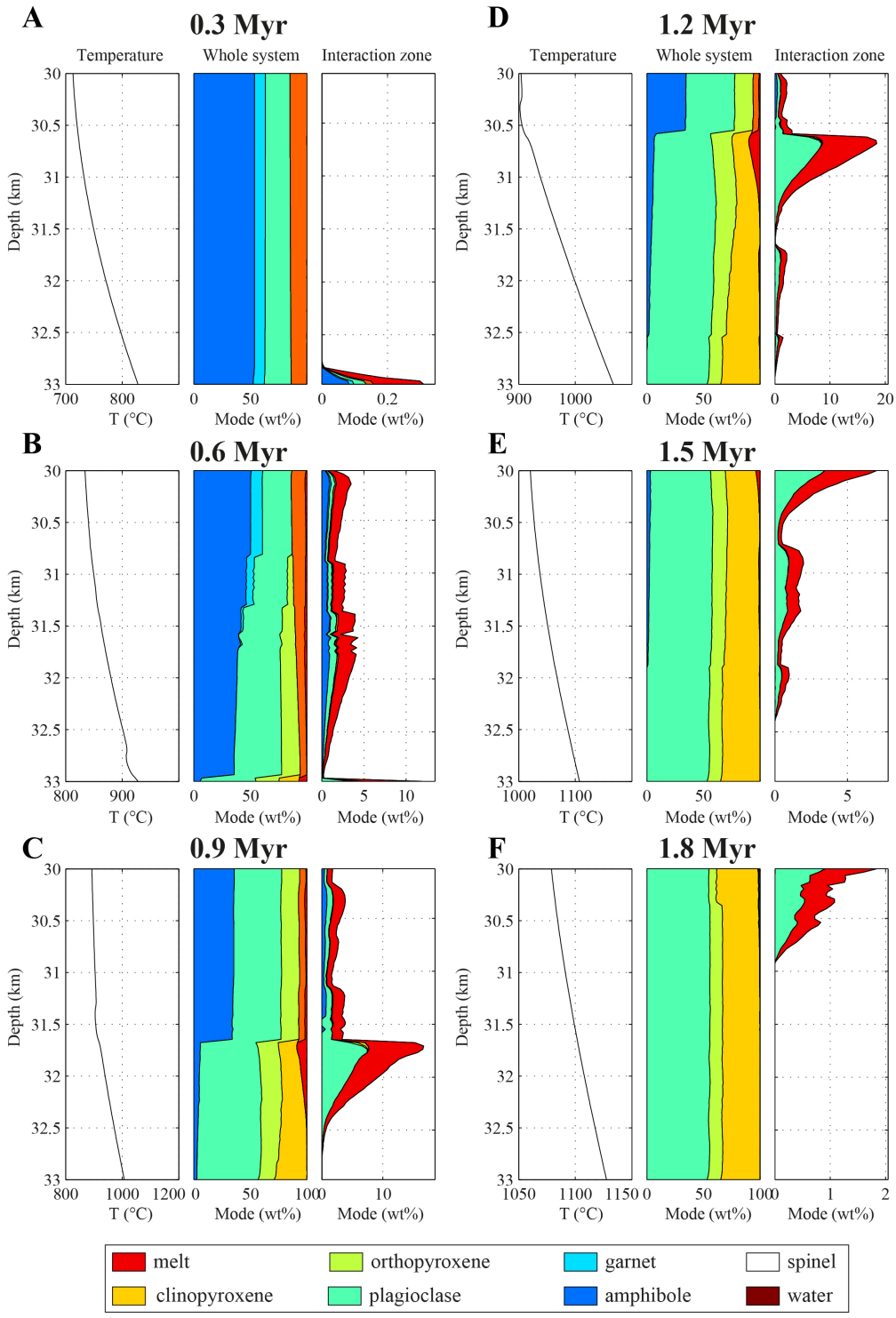

Figure 9. Modeled rate, volumes and compositions of segregated melts. A, Segregation rate. B, Cumulative thickness of segregated melt. C, Molar Mg# multiplied by 100. D to J, Na_2O, CaO, FeO, MgO, A_2O_3, SiO_2, and H_2O components, respectively.

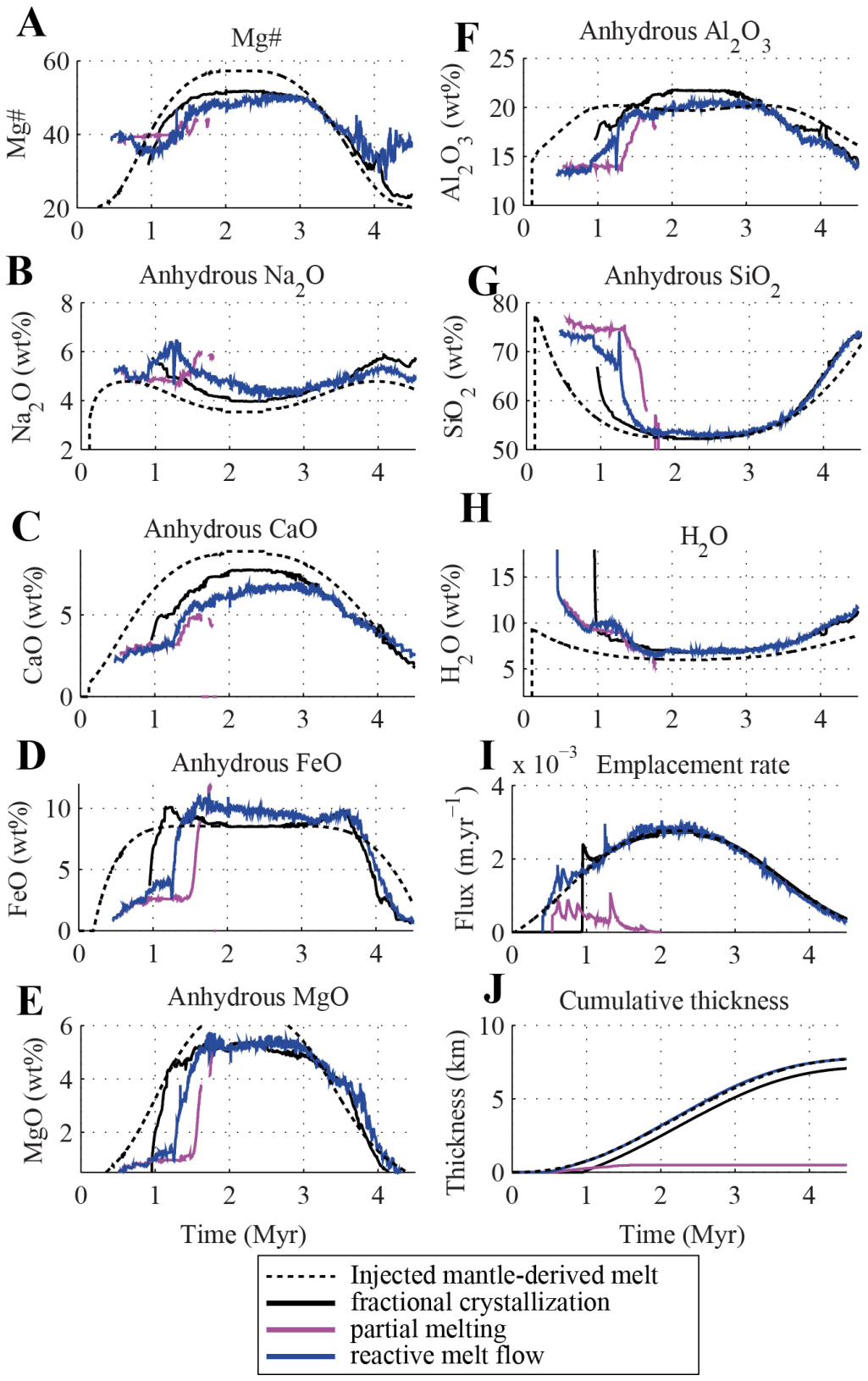

Figure 10. Mg# versus SiO_2 diagram of incoming mantle melts compared to melt output for the PM, FC and RMF models. A, Injected mantle-derived melt trend colored as function of time. B, Fractional crystallization model trend colored as function of time. C, Partial melting model trend colored as function of time. D, Reactive melt flow model trend colored as function of time. E, Comparison between incoming mantle melts (parameterized dash line) compared to melt output for the PM model (purple dots), FC model (black dots) and a fully reactive RMF model (blue dots).

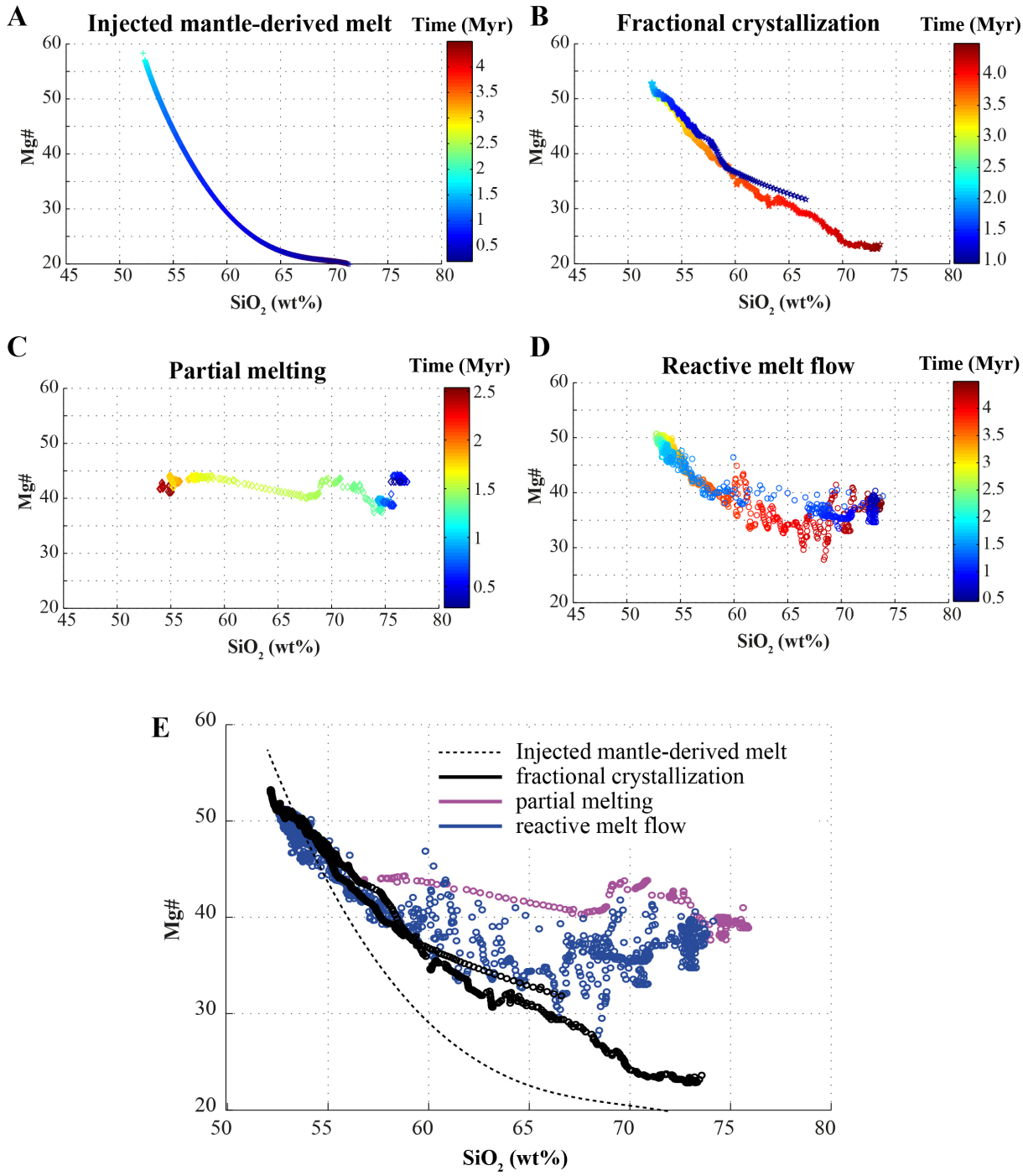

Figure 11. Results of the dynamic Fractional Crystallization model. A, B, C, temperature profile and stable phases in the interaction zone at 0.3, 0.6 and 1.2 Myr. D, Normalized evolution of the stable phases at the bottom boundary of the model. In these models the injected mantle-derived melts solely interact with their own cumulates. In this view, the host-rock can be understood as a non-reactive rock while it still carry physical properties (such as viscosity, permeability) to allow the melt to travel through. Consequently, and contrary to figures 8 and 13, the host-rock paragenesis is not shown as it is not calculated. This approach allows modeling the differentiation of the mantle-derived melt without chemical interaction with a pre-existing crust.

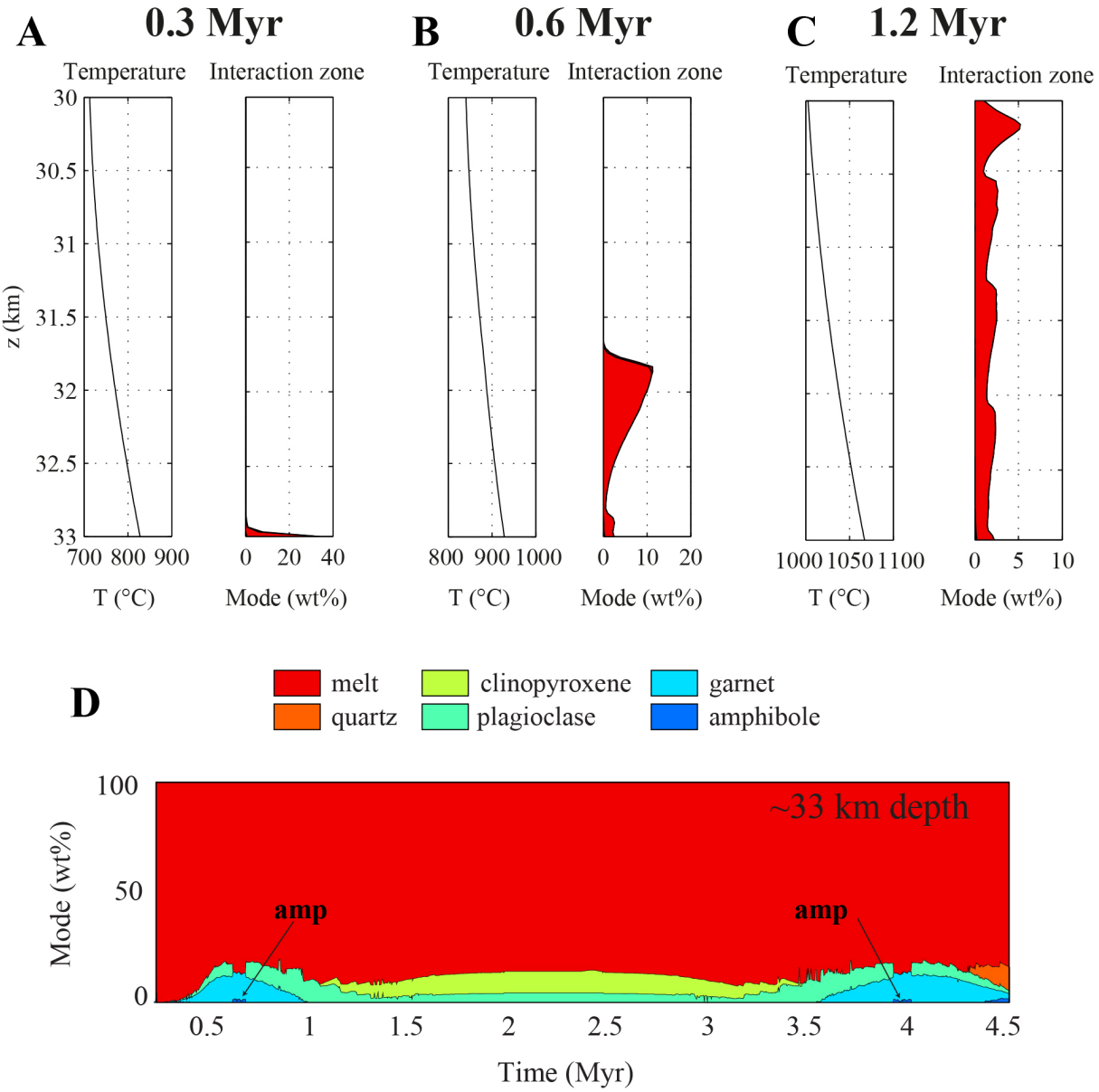

Figure 12. QAP diagram of melt output for the PM, FC and RMF models. QAP diagram after Streckeisen (1976): Q, quartz; A, orthose; P, albite + anorthite. Field 1: diorite/gabbro; 2: Q-diorite/Q-gabbro/Q-anorthosite; 3: Q-monzodiorite/Q-monzogabbro; 4: Q-Alkali-feldspar syenite; 5: alkali-feldspar syenite. Melt composition in Appendix (XX).

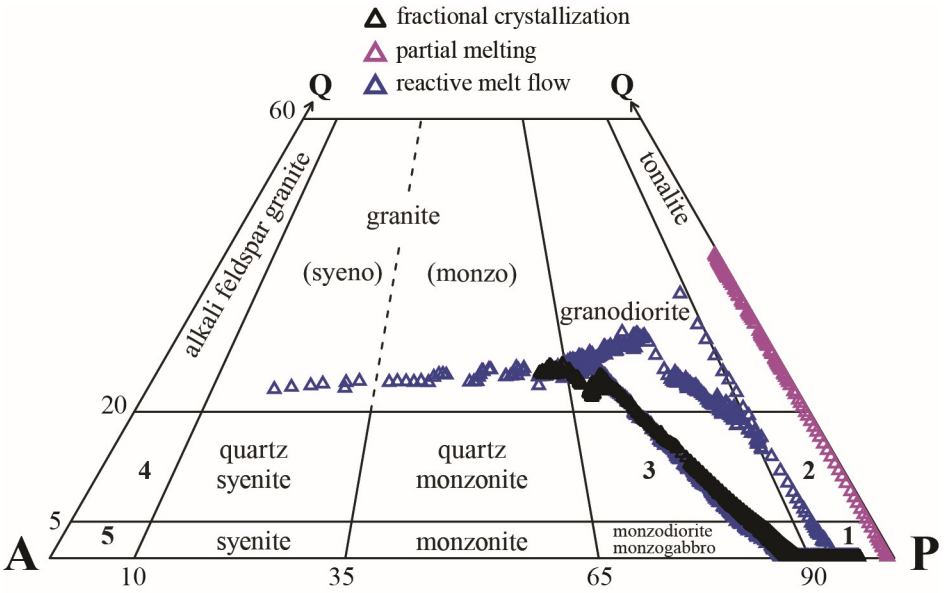

Figure 13. Stable phase evolution of the Reactive Melt Flow model. For each subfigure the left panel presents the temperature profile across the modeled section, the central panel shows the stable phases in the whole-rock and the right panel shows the stable phases in the interaction zone.

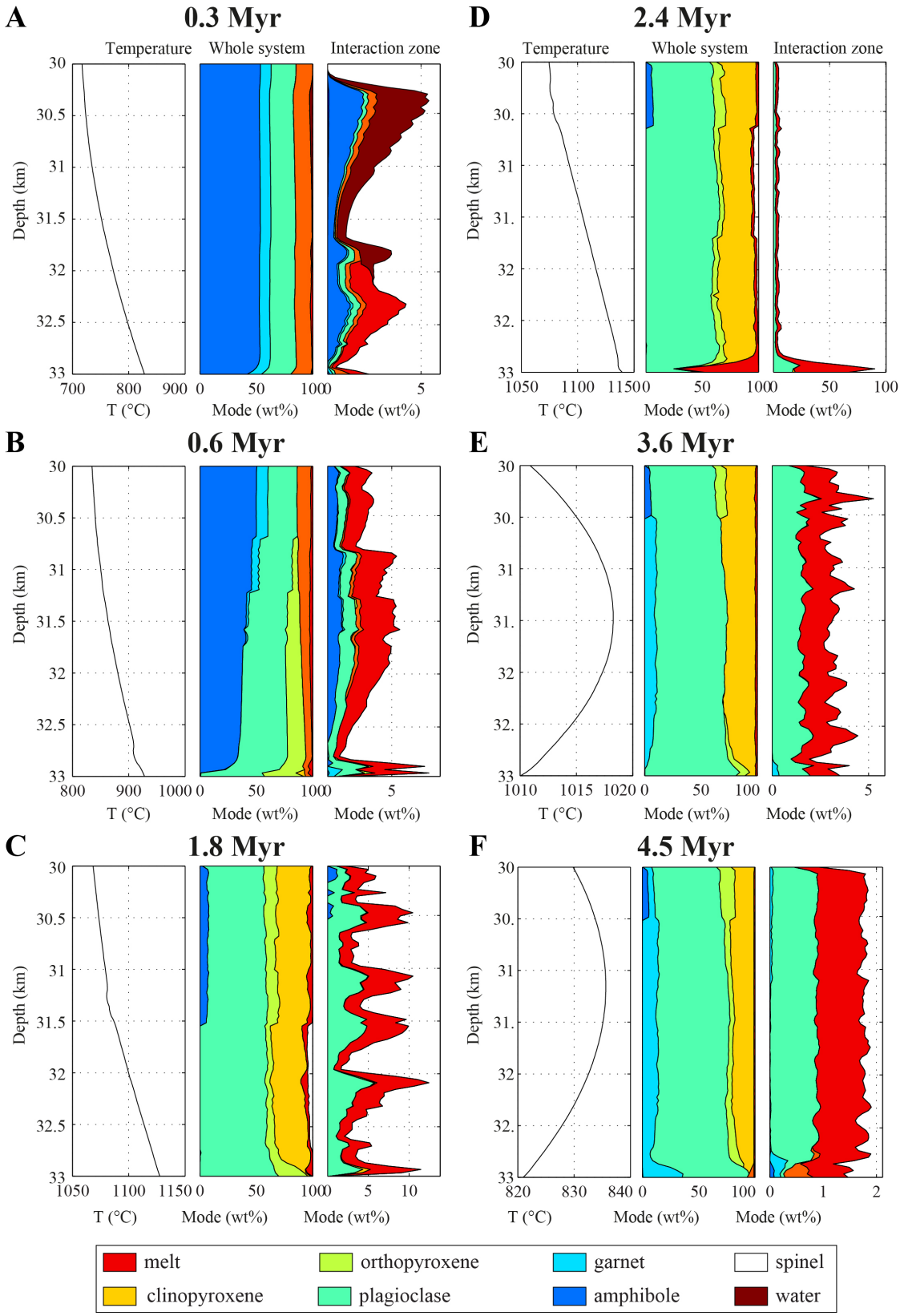

Figure 14. Melt output characteristics for the Reactive Melt Flow model through time. Black line = mantle contribution of extracted melt. Blue line = extraction rate. Dark red line = cumulative thickness of the extracted products. The main composition of the products, being felsic or intermediate, is also shown.

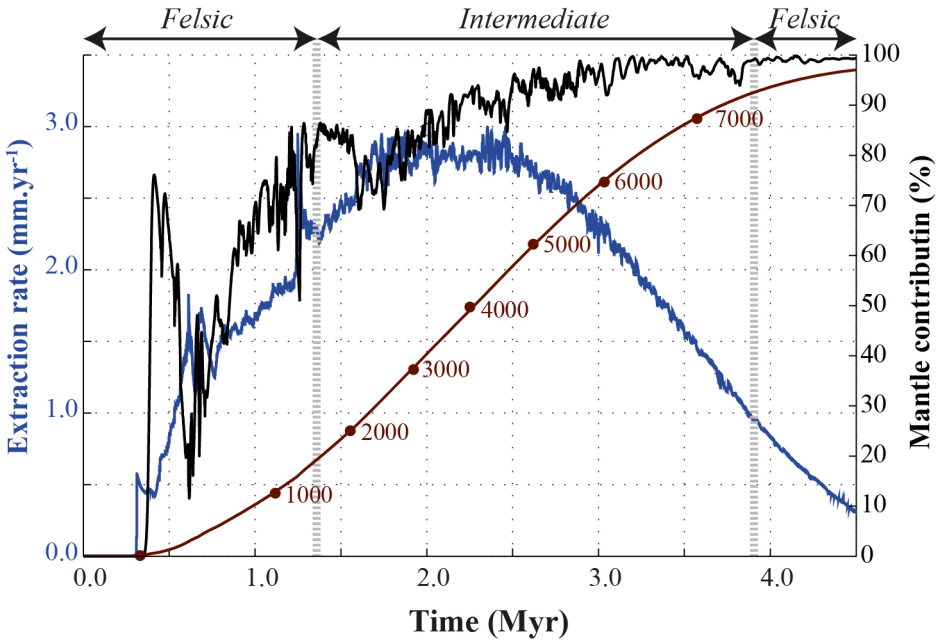

REFERENCES

Acosta-Vigil, A., D. London, and G. B. Morgan (2006), Experiments on the kinetics of partial melting of a leucogranite at 200 MPa H2O and 690–800°C: compositional variability of melts during the onset of H2O-saturated crustal anatexis, Contributions to Mineralogy and Petrology, 151(5), 539, doi:10.1007/s00410-006-0081-8.

Annen, C., J. D. Blundy, and R. S. J. Sparks (2006), The Genesis of Intermediate and Silicic Magmas in Deep Crustal Hot Zones, Journal of Petrology, 47(3), 505-539, doi:10.1093/petrology/egi084.

Balay, S., K. Buschelman, W. D. Gropp, D. Kaushik, M. G. Knepley, L. C. McInnes, B. F. Smith, and H. Zhang (2001), PETSc, See http://www. mcs. anl. gov/petsc.

Bergantz, G. W. (1989), Underplating and Partial Melting: Implications for Melt Generation and Extraction, Science, 245(4922), 1093-1095.

Bergantz, G. W., and R. Dawes (1994), Chapter 13 Aspects of Magma Generation and Ascent in Continental Lithosphere, International Geophysics, 57, 291-317, doi:http://dx.doi.org/10.1016/S0074-6142(09)60101-7.

Bouilhol, P., J. A. Connolly, and J.-P. Burg (2011), Geological evidence and modeling of melt migration by porosity waves in the sub-arc mantle of Kohistan (Pakistan), Geology, 39(12), 1091-1094.

Bouilhol, P., M. Schmidt, and J.-P. Burg (2015), Magma Transfer and Evolution in Channels within the Arc Crust: the Pyroxenitic Feeder Pipes of Sapat (Kohistan, Pakistan), Journal of Petrology, 56(7), 1309-1342.

Brown, M., Rushmer, T. (1997), The role of deformation in the movement of granite melt: views from the laboratory and the filed., In: Holness, M. B. (ed) Deformation-enhanced Fluid Transport in the Earth's Crust and Mantle. London: Chapamn and Hall, 111-144.

Brown, M. (2013), Granite: From genesis to emplacement, GSA Bulletin, 125(7-8), 1079-1113, doi:10.1130/B30877.1.

Caricchi, L., C. Annen, J. Blundy, G. Simpson, and V. Pinel (2014), Frequency and magnitude of volcanic eruptions controlled by magma injection and buoyancy, Nature Geosci, 7(2), 126-130, doi:10.1038/ngeo2041

http://www.nature.com/ngeo/journal/v7/n2/abs/ngeo2041.html#supplementary-information.

Connolly, J. (2005), Computation of phase equilibria by linear programming: a tool for geodynamic modeling and its application to subduction zone decarbonation, Earth and Planetary Science Letters, 236(1), 524-541.

Connolly, J., and Y. Podladchikov (2007), Decompaction weakening and channeling instability in ductile porous media: Implications for asthenospheric melt segregation, Journal of Geophysical Research: Solid Earth, 112(B10).

Connolly, J., and Y. Podladchikov (2015), An analytical solution for solitary porosity waves: dynamic permeability and fluidization of nonlinear viscous and viscoplastic rock, Geofluids, 15(1-2), 269-292.

Crisp, J. A. (1984), Rates of magma emplacement and volcanic output, Journal of Volcanology and Geothermal Research, 20(3), 177-211, doi:http://dx.doi.org/10.1016/0377-0273(84)90039-8.

Dale, J., R. Powell, R. White, F. Elmer, and T. Holland (2005), A thermodynamic model for Ca–Na clinoamphiboles in Na2O–CaO–FeO–MgO–Al2O3–SiO2–H2O–O for petrological calculations, Journal of Metamorphic Geology, 23(8), 771-791.

Dijkstra, A. H., M. G. Barth, M. R. Drury, P. R. D. Mason, and R. L. M. Vissers (2003), Diffuse porous melt flow and melt-rock reaction in the mantle lithosphere at a slow-spreading ridge: A structural petrology and LA-ICP-MS study of the Othris Peridotite Massif (Greece), Geochemistry, Geophysics, Geosystems, 4(8), n/a-n/a, doi:10.1029/2001GC000278.

Douce, A. E. P., and J. S. Beard (1995), Dehydration-melting of biotite gneiss and quartz amphibolite from 3 to 15 kbar, Journal of Petrology, 36(3), 707-738.

Dufek, J., and G. W. Bergantz (2005), Lower Crustal Magma Genesis and Preservation: a Stochastic Framework for the Evaluation of Basalt–Crust Interaction, Journal of Petrology, 46(11), 2167-2195, doi:10.1093/petrology/egi049.

Grove, T., S. Parman, S. Bowring, R. Price, and M. Baker (2002), The role of an H2O-rich fluid component in the generation of primitive basaltic andesites and andesites from the Mt. Shasta region, N California, Contributions to Mineralogy and Petrology, 142(4), 375-396, doi:10.1007/s004100100299.

Grove, T. L., L. T. Elkins-Tanton, S. W. Parman, N. Chatterjee, O. Müntener, and G. A. Gaetani (2003), Fractional crystallization and mantle-melting controls on calc-alkaline differentiation trends, Contributions to Mineralogy and Petrology, 145(5), 515-533, doi:10.1007/s00410-003-0448-z.

Hasalovà, P., K. Schulmann, O. Lexa, P. ŠTÍPskÁ, F. Hrouda, S. Ulrich, J. Haloda, and P. TÝCovÁ (2008), Origin of migmatites by deformation-enhanced melt infiltration of orthogneiss: a new model based on quantitative microstructural analysis, Journal of Metamorphic Geology, 26(1), 29-53, doi:10.1111/j.1525-1314.2007.00743.x.

Hashim, L., F. Gaillard, R. Champallier, N. Le Breton, L. Arbaret, and B. Scaillet (2013), Experimental assessment of the relationships between electrical resistivity, crustal melting and strain localization beneath the Himalayan–Tibetan Belt, Earth and Planetary Science Letters, 373, 20-30, doi:http://dx.doi.org/10.1016/j.epsl.2013.04.026.

Hildreth, W., and S. Moorbath (1988), Crustal contributions to arc magmatism in the Andes of central Chile, Contributions to mineralogy and petrology, 98(4), 455-489.

Holland, T., and R. Powell (1998), An internally consistent thermodynamic data set for phases of petrological interest, Journal of metamorphic Geology, 16(3), 309-343.

Jackson, M. D., M. J. Cheadle, and M. P. Atherton (2003), Quantitative modeling of granitic melt generation and segregation in the continental crust, Journal of Geophysical Research: Solid Earth, 108(B7), n/a-n/a, doi:10.1029/2001JB001050.

Jackson, M. D., K. Gallagher, N. Petford, and M. J. Cheadle (2005), Towards a coupled physical and chemical model for tonalite–trondhjemite–granodiorite magma formation, Lithos, 79(1–2), 43-60, doi:http://dx.doi.org/10.1016/j.lithos.2004.05.004.

Jagoutz, O., and P. B. Kelemen (2015), Role of arc processes in the formation of continental crust, Annual Review of Earth and Planetary Sciences, 43, 363.

Jagoutz, O., O. Müntener, J. P. Burg, P. Ulmer, and E. Jagoutz (2006), Lower continental crust formation through focused flow in km-scale melt conduits: The zoned ultramafic bodies of the Chilas Complex in the Kohistan island arc (NW Pakistan), Earth and Planetary Science Letters, 242(3), 320-342, doi:http://dx.doi.org/10.1016/j.epsl.2005.12.005.

Jennings, E. S., and T. J. B. Holland (2015), A Simple Thermodynamic Model for Melting of Peridotite in the System NCFMASOCr, Journal of Petrology, 56(5), 869-892, doi:10.1093/petrology/egv020.

Keller, T., D. A. May, and B. J. P. Kaus (2013), Numerical modelling of magma dynamics coupled to tectonic deformation of lithosphere and crust, Geophysical Journal International, 195(3), 1406-1442, doi:10.1093/gji/ggt306.

Kemp, A. I. S., C. J. Hawkesworth, G. L. Foster, B. A. Paterson, J. D. Woodhead, J. M. Hergt, C. M. Gray, and M. J. Whitehouse (2007), Magmatic and Crustal Differentiation History of Granitic Rocks from Hf-O Isotopes in Zircon, Science, 315(5814), 980-983, doi:10.1126/science.1136154.

Leitch, A., and R. Weinberg (2002), Modelling granite migration by mesoscale pervasive flow, Earth and Planetary Science Letters, 200(1), 131-146.

McKenzie, D. (1984), The Generation and Compaction of Partially Molten Rock, Journal of Petrology, 25(3), 713-765, doi:10.1093/petrology/25.3.713.

McKenzie, D. (1985), The extraction of magma from the crust and mantle, Earth and Planetary Science Letters, 74(1), 81-91, doi:http://dx.doi.org/10.1016/0012-821X(85)90168-2.

Miller, R. B., and S. R. Paterson (1999), In defense of magmatic diapirs, Journal of Structural Geology, 21(8), 1161-1173, doi:http://dx.doi.org/10.1016/S0191-8141(99)00033-4.

Müntener, O., and P. Ulmer (2006), Experimentally derived high-pressure cumulates from hydrous arc magmas and consequences for the seismic velocity structure of lower arc crust, Geophysical Research Letters, 33(21).

Newton, R., and H. Haselton (1981), Thermodynamics of the garnet—plagioclase—Al2SiO5—quartz geobarometer, in Thermodynamics of minerals and melts, edited, pp. 131-147, Springer.

Paterson, S. R., and O. T. Tobisch (1992), Rates of processes in magmatic arcs: implications for the timing and nature of pluton emplacement and wall rock deformation, Journal of Structural Geology, 14(3), 291-300, doi:http://dx.doi.org/10.1016/0191-8141(92)90087-D.

Paterson, S. R., and R. H. Vernon (1995), Bursting the bubble of ballooning plutons: A return to nested diapirs emplaced by multiple processes, GSA Bulletin, 107(11), 1356-1380, doi:10.1130/0016-7606(1995)107<1356:BTBOBP>2.3.CO;2.

Petford, N. (1996), Dykes or diapirs?, Geological Society of America Special Papers, 315, 105-114.

Petford, N. (2003), Rheology of granitic magmas during ascent and emplacement, Annual Review of Earth and Planetary Sciences, 31(1), 399-427.

Qian, Q., and J. Hermann (2013), Partial melting of lower crust at 10–15 kbar: constraints on adakite and TTG formation, Contributions to Mineralogy and Petrology, 165(6), 1195-1224.

Rapp, R. P., and E. B. Watson (1995), Dehydration melting of metabasalt at 8–32 kbar: implications for continental growth and crust-mantle recycling, Journal of Petrology, 36(4), 891-931.

Reubi, O., and J. Blundy (2009), A dearth of intermediate melts at subduction zone volcanoes and the petrogenesis of arc andesites, Nature, 461(7268), 1269-1273.

Richard, G. L., and S. L. Gavrilyuk (2015), Modelling turbulence generation in solitary waves on shear shallow water flows, Journal of Fluid Mechanics, 773, 49-74, doi:10.1017/jfm.2015.236.

Riel, N., J. Mercier, and R. Weinberg (2016), Convection in a partially molten metasedimentary crust? Insights from the El Oro complex (Ecuador), Geology, 44(1), 31-34, doi:10.1130/G37208.1.

Rosenberg, C., and M. Handy (2005), Experimental deformation of partially melted granite revisited: implications for the continental crust, Journal of metamorphic Geology, 23(1), 19-28.

Rutter, E. H., and J. Mecklenburgh (2006), The extraction of melt from crustal protoliths and the flow behaviour of partially molten crustal rocks: An experimental perspective, Citeseer.

Scaillet, B., F. Holtz, and M. Pichavant (1997), Rheological Properties of Granitic Magmas in Their Crystallization Range, in Granite: From Segregation of Melt to Emplacement Fabrics, edited by J. L. Bouchez, D. H. W. Hutton and W. E. Stephens, pp. 11-29, Springer Netherlands, Dordrecht, doi:10.1007/978-94-017-1717-5_2.

Schoene, B., U. Schaltegger, P. Brack, C. Latkoczy, A. Stracke, and D. Günther (2012), Rates of magma differentiation and emplacement in a ballooning pluton recorded by U-Pb TIMS-TEA, Adamello batholith, Italy, Earth and Planetary Science Letters, 355-356, 162-173, doi:10.1016/j.epsl.2012.08.019.

Sen, C., and T. Dunn (1994), Dehydration melting of a basaltic composition amphibolite at 1.5 and 2.0 GPa: implications for the origin of adakites, Contributions to Mineralogy and Petrology, 117(4), 394-409.

Shaw, H. R. (1980), The fracture mechanisms of magma transport from the mantle to the surface, Physics of magmatic processes, 64, 201-264.

Sisson, T., K. Ratajeski, W. Hankins, and A. F. Glazner (2005), Voluminous granitic magmas from common basaltic sources, Contributions to Mineralogy and Petrology, 148(6), 635-661.

Solano, J. M. S., M. D. Jackson, R. S. J. Sparks, J. D. Blundy, and C. Annen (2012), Melt Segregation in Deep Crustal Hot Zones: a Mechanism for Chemical Differentiation, Crustal Assimilation and the Formation of Evolved Magmas, Journal of Petrology, doi:10.1093/petrology/egs041.

Solano, J. M. S., M. D. Jackson, R. S. J. Sparks, and J. Blundy (2014), Evolution of major and trace element composition during melt migration through crystalline mush: Implications for chemical differentiation in the crust, American Journal of Science, 314, 895-939. doi:10.2475/05.2014.01

Soustelle, V., A. Tommasi, J. L. Bodinier, C. J. Garrido, and A. Vauchez (2009), Deformation and Reactive Melt Transport in the Mantle Lithosphere above a Large-scale Partial Melting Domain: the Ronda Peridotite Massif, Southern Spain, Journal of Petrology, 50(7), 1235-1266, doi:10.1093/petrology/egp032.

Streckeisen, A.L. (1976), Classification and Nomenclature of Igneous Rocks. N. Jahrb. Miner. Abh., 107, 144-240.Stuart, C. A., Piazolo, S. and Daczko, N.R. (2016), Mass transfer in the lower crust: evidence for incipient melt assisted flow along grain boundaries in the deep arc granultes of Fiordland, New Zealand, Geochemistry, Geophysics, Geosystems (G3), doi:10.1002/2015GC006236.

Vigneresse, J. L., P. Barbey, and M. Cuney (1996), Rheological Transitions During Partial Melting and Crystallization with Application to Felsic Magma Segregation and Transfer, Journal of Petrology, 37(6), 1579-1600, doi:10.1093/petrology/37.6.1579.

von Bargen, N., and H. S. Waff (1986), Permeabilities, interfacial areas and curvatures of partially molten systems: Results of numerical computations of equilibrium microstructures, Journal of Geophysical Research: Solid Earth, 91(B9), 9261-9276, doi:10.1029/JB091iB09p09261.

Voss, M., and W. Jokat (2007), Continent-ocean transition and voluminous magmatic underplating derived from P-wave velocity modelling of the East Greenland continental margin, Geophysical Journal International, 170(2), 580-604.

Walker, J. B. A., G. W. Bergantz, J. E. Otamendi, M. N. Ducea, and E. A. Cristofolini (2015), A MASH Zone Revealed: the Mafic Complex of the Sierra Valle Fértil, Journal of Petrology, 56(9), 1863-1896, doi:10.1093/petrology/egv057.

Weinberg, R. F. (1999), Mesoscale pervasive felsic magma migration: alternatives to dyking, Lithos, 46(3), 393-410.

Wickham, S. M. (1987), The segregation and emplacement of granitic magmas, Journal of the Geological Society, 144(2), 281-297, doi:10.1144/gsjgs.144.2.0281.

Wolf, M., and P. Wyllie (1991), Dehydration-melting of solid amphibolite at 10 kbar: textural development, liquid interconnectivity and applications to the segregation of magmas, Mineralogy and Petrology, 44(3-4), 151-179.

Zhang, C., F. Holtz, J. Koepke, P. E. Wolff, C. Ma, and J. H. Bédard (2013), Constraints from experimental melting of amphibolite on the depth of formation of garnet-rich restites, and implications for models of Early Archean crustal growth, Precambrian Research, 231, 206-217.

Parameter	Symbol	Value	Unit
Background porosity	φ_0	10^{-3}	
Background permeability	k_0	10^{-6}	m²
Porosity exponent	n	3	
Host-rock bulk viscosity	η_s	10^{19}	Pa.s
Melt viscosity	η_f	10^{3}	Pa.s
Density contrast	$\Delta\rho$	$\rho_s - \rho_f$	$kg.m^{-3}$
Gravity acceleration	g	9.81	$m.s^{-2}$
Temperature function constants	C_1	1005.0	
	C_2	21.43	
	C_3	-99.0	
	t_{max}	4.0×10^{6}	yrs
Average heat capacity	Cp^{mean}	10^{3}	$J.K^{-1}$
Heat diffusivity	κ	10^{-6}	$m^2.s^{-1}$
Latent heat of melting/crystallization	H	4×10^{5}	$J.kg^{-1}$
Petrological timestep	-	10^{3}	yrs
Two-phase flow timestep	-	10^{2}	yrs
Lithostatic pressure at top boundary	P_{top}	0.9	GPa
Model thickness	Δz	3.0	km
Rate of mantle-derived melt injection	$\vec{q}_{basalt}$	4.0	$mm.yr^{-1}$
Melt/rock ratio	-	1:1	

Table 1. Parameters used in the models

Oxide	anhydrous content (wt%)
Na_2O	2.35
CaO	8.90
FeO	8.15
MgO	6.77
Al_2O_3	15.22
SiO_2	48.55
H_2O	1.0

Table 2. Amphibolite composition. MIX-B Composition in the NCFMASH system after Qian et al. (2013).

Content (wt%)	C0	C1	C2	C3	C4	C5	x
Melt	109.63	-0.34779	0.00027375	-	-	-	-
Na_2O	4.5819	-0.69613	-0.79349	-0.12051	0.14484	0.1173	(T-1019.2)/151.74
CaO	6.284	3.7298	-0.27611	-0.37158	-	-	(T-1017.7)/149.28
K_2O	1.6378	-1.9878	0.58347	0.36578	-0.1528	-	(T-1017.7)/149.28
FeO	8.1943	1.4409	-1.5685	0.4794	-	-	(T-1020)/145.75
MgO	2.9781	3.6742	1.4723	-0.25709	-0.0363	-	(T-1020)/145.75
Al_2O_3	19.581	2.4595	-1.7746	-0.84363	-	-	(T-997.14)/164.08
SiO_2	56.326	-6.7803	2.7099	-	-	-	(T-1020)/145.75
H_2O	26.825	-0.03	1062100	-	-	-	-

Table 3. Polynomial regression for mantle-derived melt. Where T is the temperature in °C and C0 to C5 are the constants multiplying the x^0 to x^5.